ANGULAR DEPENDENT VORTEX DYNAMICS IN SUPERCONDUCTORS WITH COLUMNAR DEFECTS

LEONARDO CIVALE
Superconductivity Technology Center,
Los Alamos National Laboratory, Los Alamos, NM 87545, USA.

ALEJANDRO V. SILHANEK
Laboratorium voor Vaste-Stoffysica en Magnetisme,
K. U. Leuven, Celestijnenlaan 200D, B-3001 Leuven, Belgium.

GABRIELA PASQUINI
Laboratorio de Bajas Temperaturas, Departamento de Física,
Facultad de Ciencias Exactas y Naturales,
Universidad de Buenos Aires, Buenos Aires, Argentina.

I. INTRODUCTION

A. Motivation

The introduction of aligned columnar defects (CD) in high temperature superconductors (HTSC) was initially motivated[1] by the technological objective of increasing the discouragingly low vortex pinning of the early samples of these compounds. Initial results clearly showed[1, 2] that CD were extremely effective in improving the critical current density (J_c) (particularly at high temperatures and magnetic fields) and in enhancing the irreversibility field (H_{irr}). In addition, it soon became clear[3, 4] that good quality single crystals with CD were excellent "model systems" to explore the complexities of vortex dynamics in HTSC. The combination of both motivations produced a very large interest on the topic[5], which remains active after more than a decade of research.

Vortex pinning in type II superconductors arises[4, 6] from the presence of crystalline defects, which produce a spatially inhomogeneous superconducting order parameter $\psi(\mathbf{r})$, thus inducing a position dependent vortex energy. Examples of those defects are dislocations, chemical doping, vacancies, non superconducting particles, voids, etc. The calculation of the expected J_c as a function of temperature (T) and magnetic induction ($\mathbf{B}$) is a very complex problem[4, 6], as it depends nontrivially on a large number of variables such as the nature of the defects, their size, shape and density, as well as on the temperature and magnetic field dependent elastic properties of the vortex array, which in turn are determined by the superconducting parameters of the material. If the material and/or the defects are anisotropic, pinning will additionally depend on the orientation of the applied magnetic field $\mathbf{H}$.

A particularly important type of anisotropic pinning is that produced by extended parallel pinning potentials, commonly known as correlated pinning[3]. In HTSC, common examples

of correlated pinning structures are the CD, the twin boundaries[7, 8, 9, 10, 11], and the layered crystallographic structure of these materials that produces the intrinsic pinning[12, 13]. Although each one has its distinctive characteristics (CD are linear while the other two are planar, intrinsic pinning potentials are spatially periodic while the separation between CD and twins is random), they share several important similarities in their pinning properties, particularly in regards to the vortex structures that occur[3, 4] as a function of the orientation of **H**. In all cases, pinning is maximum when the vortices are parallel to the defects. They all exhibit a lock-in phase: when the angle φ between **H** and the defects is smaller than a certain lock-in angle φ_L, the vortex cores remain locked into the pinning potentials. For $\varphi > \varphi_L$, vortices form staircases, with core segments locked into the defects connected by weakly pinned kinks.

Different mechanisms can produce aligned linear defects capable of pinning vortices in a superconductor. In $YBa_2Cu_3O_7$ (YBCO), for instance, pinning by dislocations[14, 15] and by the lines occurring at the intersection of two perpendicular families of twins[16] has been explored. However, we will restrict the term "columnar defect" to those produced by irradiation with very energetic heavy-ions. Several features set them apart from the rest. First, they can produce a much larger J_c than any other types of linear defects (as discussed in section I.C. below, this is mainly due to the fact that CD have the appropriate diameter). Second, their density can be easily controlled. Third, they can be introduced at an arbitrary crystalline orientation. This is a unique advantage of the CD as a tool to explore vortex dynamics, as it allows to deconvolute the features arising from their uniaxial pinning from those due to anisotropy and other correlated pinning mechanisms. We also note that by "aligned" CD we do not mean that all the tracks are perfectly parallel, as will be discussed in the next three subsections. We just use this term as opposite to CD purposely generated with high angular dispersion[17, 18] (splay) or even randomly oriented[19, 20].

The purpose of this review is to discuss the angular dependence of the vortex dynamics in type II superconductors with aligned CD. The problem is rather complex, and some aspects still require further investigation. Our main goal is to identify and characterize the various angular regimes, both statically and dynamically. To that end we will use and combine results obtained by dc magnetization and ac susceptibility measurements. We will show that both the crystalline anisotropy and geometrical anisotropy (sample shape) play an important role. Most of our studies have been performed on high quality twinned YBCO single crystals prepared using a flux growth technique [21]. In this compound, the combined effects of the three types of correlated pinning mechanisms and the anisotropy produce a rich variety of vortex structures and dynamic responses. Complementary studies were performed on high quality single crystals[22] of the less anisotropic conventional superconductor $NbSe_2$, with $T_c = 7.3$ K, coherence length $\xi = 77$ Å, and penetration depth $\lambda = 690$ Å, and having the c axis parallel to the thinnest dimension. Magnetization and susceptibility measurements were performed at the Centro Atómico Bariloche and Centro Atómico Constituyentes respectively, both dependent on the Atomic Energy Commission of Argentina.

This review is organized as follows: In the remaining of section I, we briefly describe the generation of CD by heavy-ion irradiation (section I.B), and we summarize the basic vortex dynamics for superconductors with aligned CD (the case **H** $\parallel$ CD is discussed in I.C., and the angular dependence in I.D.). In section II we present an overview of the temperature, field and angular dependence of the irreversible magnetization in samples with columnar defects and analyze the influence of correlated defects on the pinning properties of vortex lines. First (in section II.A.) we discuss the origin of the irreversible magnetization

in superconductors and introduce our measurement procedures. In section II.B. we focus on the angular regimes associated with different vortex configurations as the external field is tilted away from the CD orientation. In section II.C. we show that the sample geometry and the material anisotropy are competing mechanisms that determine the vortex orientation at low fields. In section III we use our ac susceptibility measurements to explore the vortex dynamics in YBCO with CD in the vicinity of the solid-liquid boundary. In section III.A. we introduce the experimental procedure. In section III.B. we study the angular dependence of the ac response with the scope to identify the various angular regimes and to investigate which is the main source of pinning at different orientations of a low DC field. In section III.C. we explore the dynamic response of vortices aligned with the CD over a wide range of current densities and excitation frequencies, and we construct the dynamic phase diagram of the system in the temperature vs ac field plane. In section III.D. we extend that study to different angles between the applied field and the tracks.

B. The generation of CD by heavy-ion irradiation

The generation of CD by irradiation with very energetic heavy ions has been extensively discussed in the literature (for a review see for example ref. 5 and references therein). Here we will only present a very brief summary of the basic concepts.

Particle irradiation is a standard way to introduce defects in a solid. Incident particles transfer energy to a solid[23, 24, 25] by direct collisions with lattice atoms (nuclear or nonionizing energy loss, S_n), and by ionization or electronic excitations (electronic or ionizing energy loss, S_e). In the case of irradiation with electrons, protons and light ions with energies up to a few MeV, almost all the energy is transferred via nonionizing energy loss[23]. This results in defect formation through displacement of the primary recoil atom, and through the cascade of collisions that this atom produces if its energy is high enough[25]. The size of the damaged region increases with the primary recoil energy transfer. Electron irradiation (up to a few MeV) can only produce point defects (vacancy-interstitial pairs or Frenkel pairs), while protons and light ions generate defects up to several tens of Å in size. Fast neutrons also generate cascade defects, with diameters in the range of 50 to 100 Å. In all cases, these defects are randomly distributed.

As heavier and more energetic ions are considered, S_e grows and the electronic energy loss becomes dominant[24]. For instance, for our typical irradiations using $\sim$ 300 MeV Au, $S_e \sim 100 S_n$, while for ion energies in the GeV range the relation can be as large[26] as $S_e \sim 2000 S_n$. In this limit each incident ion forms a cylinder of amorphyzed material along its path, around 40 to 100 Å in diameter, known as a latent track. The heavier and more energetic the ion, the more continuous, homogeneous and parallel are the tracks. In fact, as S_e increases the defects evolve[26, 27] from isolated uncorrelated spheres to aligned spheres, then to elongated aligned but disconnected defects, which then coalesce into discontinuous inhomogeneous tracks, which eventually become continuous and finally homogeneous. However, as will be pointed out below, perfectly aligned and homogeneous defects are not necessarily the best suited for high vortex pinning.

The S_e values separating the various regimes depend on the material. The thresholds are lowest in insulators, while in the other extreme it is impossible to create continuous tracks in good metals. For the case of YBCO, irradiation with 173 MeV Xe ($S_e \sim 1.2$ KeV/Å), for instance, does not generate defects capable to produce uniaxial pinning. In this material, the threshold for the formation of continuous inhomogeneous tracks is[28] $S_e \sim 2$ KeV/Å,

somewhat below the 2.7 KeV/Å that occurs at the entry surface for the 580 MeV Sn^{30+} used[1] in the initial studies. Heavier ions such as Au and Pb in the GeV energy range, which have S_e as high[28] as 3.5 to 4.5 KeV/Å, result in homogeneous tracks. All these S_e values are extremely large, so incident ions lose energy very fast as they penetrate deeper into the target. As they do, at some point S_e starts to decrease, so the morphology of every track changes as a function of depth, until the ion is eventually stopped. Typical range of continuous tracks formation is about 10 μm for our 300 MeV Au, and can be as large as $\sim$ 100 μm for energies in the several GeV range. As ions penetrate deeper into the material, the angular dispersion of the tracks also increases[29]. This is mainly due to Rutherford scattering of the incident ions, associated to the small but nonzero nuclear energy loss. A completely different approach based on fission tracks can be used[19, 20] to generate randomly oriented CD.

Irradiations reported in this review were performed at room temperature at the TANDAR accelerator facility. A group of samples was irradiated with 291 MeV Au^{27+} ions and another one with 220 MeV Sn^{22+} ions. In both cases, the energy deposition rate is greater than the threshold for continuous latent track formation in the first $9-10$ μm. So we only used crystals of thickness ≤ 10 μm.

C. Vortex dynamics in superconductors with CD: basic results for H $\parallel$ CD

In this subsection we present a brief summary of the basic results of vortex dynamics when the applied magnetic field is parallel to the CD. More detailed theoretical analyses can be found in refs. 3 and 4.

The basic reason why CD are very effective pinning centers when the vortex direction is parallel to them is quite simple: each CD can in principle confine the whole length of the vortex core, thus producing the maximum possible pinning energy without any cost in elastic energy due to vortex bending. This contrasts with the case of randomly distributed defects, where only a fraction of the core length is pinned, and additionally vortices must zig-zag among defects in order to get pinned, thus paying an additional price in terms of vortex elastic energy.

Let's start with a rough estimate. At low temperatures and for an isolated vortex (*i.e.*, at low enough fields) the pinning energy per unit length of a CD (assuming $\psi = 0$ inside it) is $\varepsilon_p \sim (H_c^2/8\pi)\pi b^2$, where H_c is the thermodynamic critical field and b is the smallest of the defect radius r_D and the core radius $\sqrt{2}\xi$ (here ξ is the superconducting coherence length). The pinning force per unit length will be of the order of $F_p \sim \varepsilon_p/\xi$, and the critical current density $J_c = cF_p/\Phi_0$, where Φ_0 is the flux quantum and c is the speed of light. Clearly, the most convenient case is $r_D \sim \sqrt{2}\xi$, so the highest F_p is achieved without removing more superconducting material than necessary. In this case we obtain $J_c \sim J_0/2$, where $J_0 = cH_c/3\sqrt{6}\pi\lambda$ is the depairing current and λ is the superconducting penetration depth for $\mathbf{H} \parallel c$ axis. A more exact calculation gives[3, 4] $J_c \sim \left(3\sqrt{3}/4\sqrt{2}\right) J_0 \sim J_0$, showing that, at least in principle, CD can produce a J_c pretty close to the maximum theoretically achievable value. It is a fortunate fact that the CD produced by heavy-ion irradiation have a radius $\sim 20-50$ Å that matches very well with the vortex core radius $\sqrt{2}\xi \sim 25$ Å of HTSC. On the other hand, the reality is that the largest J_c's measured[5], at low temperatures in YBCO crystals with CD are $\sim 4-5\times 10^7$ A/cm^2. Although these values are very high, they are far from the ideal limit $\sim J_0(T=0) \sim 3\times 10^8$ A/cm^2. This may be due to a variety of factors related to the morphology of the tracks, such as its inhomogeneities, the

degree of depression of ψ, the sharpness of the normal/superconducting boundary, etc. It is thus useful to introduce[30] a dimensionless *efficiency factor* $\eta \leq 1$ in the pinning estimates, which accounts for all the uncertainties mentioned.

Several additional factors reduce ε_p (and thus J_c) as temperature increases[3, 4]. First, $H_c(T)$ decreases with T. Second, as $\xi(T)$ increases with T a crossover from $r_D > \sqrt{2}\xi$ to $r_D < \sqrt{2}\xi$ may occurs. The third and most important factor is due to thermal fluctuations and is known as entropic smearing. The transverse localization length of the vortex cores, which is determined by the root mean square amplitude of the thermal fluctuations, grows as $k_B T$, thus reducing the vortex free energy $F = U - TS$ due to the increase of the entropy S arising from the delocalization. As a consequence, the effective potential well associated to the CD becomes "shallow" and the pinning energy decreases by a factor $f(x)$, where $f(x) \sim \exp(-x)$ for $x > 1$, according to the long range nature of the CD-vortex interaction[4]. Here $x = T/T_{dp}$ and T_{dp} is called the depinning temperature. In the very useful analogy to 2D-bosons[3], this corresponds to the decrease in binding energy of a quantum well due to the zero-point fluctuations. The entropic smearing effect has been experimentally observed in YBCO, and it was found[30, 31] that $T_{dp} \sim 40$ K. The combination of all the factors mentioned above produce an *effective* pinning energy per unit length

$$\varepsilon_p(T) = \eta \frac{\varepsilon_0}{2} \ln\left(1 + \frac{r^2}{2\xi^2}\right) \times f(x) \tag{1}$$

where $\varepsilon_0(T) = (\Phi_0/4\pi\lambda)^2$ is the vortex energy scale, and the logarithmic factor provides a convenient interpolation[4] between the $r_D > \sqrt{2}\xi$ and $r_D < \sqrt{2}\xi$ cases.

As the vortex density increases, more CD will be occupied. The natural characteristic field in the problem is[1] the matching field $B_\Phi = n\Phi_0$, where n is the areal density of CD. For $B \gg B_\Phi$ there are many more vortices than CD, so all the CD are occupied and only a small fraction $\sim B/B_\Phi$ of the flux lines are actually trapped, the rest of them being pinned only as a result of vortex-vortex interactions. We thus expect J_c to decrease fast with B in this regime, as indeed observed[1, 5, 30]. When $B \ll B_\Phi$ each flux line will be confined into a CD. However, as B increases it may occur that, although there is a CD available, it will be energetically unfavorable for the vortex to occupy it because it is too close to another vortex, so the gain in pinning energy will be overcompensated by the increase in the elastic energy associated to the vortex-vortex repulsion. The characteristic field where this effect sets in is called the *accommodation field*, $B_a(T) \propto (\varepsilon_p(T)/\varepsilon_0)\, B_\Phi$, which represents the crossover between single vortex pinning where vortex interactions are negligible and collective pinning where they become significant[3, 4, 30]. At low temperatures B_a approaches B_Φ, but above T_{dp} it decreases due to the reduction in $\varepsilon_p(T)$. Above a temperature $T_{dl} > T_{dp}$ the localization length becomes larger than the average distance between tracks, so vortices become collectively pinned by several tracks and $B_a(T)$ decreases faster. We have estimated[32] that in YBCO $T_{dl} \sim 70$K.

Thermal fluctuations are also responsible for the large flux creep in HTSC. In the presence of CD and below $B_a(T)$, initial relaxation proceeds via nucleation and expansion of half loops[3, 4, 33]. This is a glassy regime, in the sense that the current density dependent *activation energy* $U(J)$ increases as J^{-1} with decreasing current density. Below a certain J, a crossover to a creep regime dominated by double kinks occurs[33]. These excitations involve the transfer of a flux line from one CD to another one, and once a double kink is formed its further expansion is energetically favorable, thus relaxation in this regime is fast and *nonglassy*. Below a still lower J, the expansion of double kinks is precluded by

the dispersion in the pinning energy of the CD. Relaxation now evolves through another type of excitations called superkinks. This regime, analogous to the variable range hopping conductivity in doped semiconductors, is again glassy, with $U(J)$ diverging as $J^{-1/3}$. For $B > B_a(T)$ intervortex interactions are relevant at all current densities, and the relaxation takes place via collective excitations involving vortex bundles. A description of the relaxation regimes in that case can be found in Ref. 4.

An interesting implication of the above analysis is that identical and perfectly parallel CD are not the ideal configuration to sustain large persistent current densities, because they allow for the fast, nonglassy relaxation of double kinks[3, 4, 33]. In fact, it has been theoretically predicted[34], and experimentally demonstrated[18, 29], that larger persistent currents can be obtained in the case of CD having a small angular dispersion or splay. The case of very large angular splay is also interesting and has been explored by generating randomly oriented fission tracks[19, 20].

A related phenomenon is the matching effect. When $B = B_\Phi$, the available phase space for transfer of vortex cores between two CD should be strongly limited. Thus, creep rate should be reduced and the field dependence of the persistent current should exhibit a peak at B_Φ. However, this matching effect is generally not observed[1, 5]. The reason is that usually the energy and angle dispersion of the CD reduces the creep at all fields[35], thus masking this phenomenon. Matching effects have only been observed[35, 36] in very thin samples containing CD with very low energy and angle dispersion.

D. Angular dependence: Bose glass picture

Our studies of the angular dependence of vortex pinning in HTSC with CD have revealed a richer variety of phenomena and pinning regimes than originally expected. As we will extensively discuss in the following sections, this is due to a number of additional ingredients such as influence of other types of correlated disorder, energy dispersion of the CD and misalignments between **B** and **H** due to both mass anisotropy and sample shape. But first, in this subsection we briefly summarize the expectations within the basic Bose Glass scenario[3, 4] for a single family of identical and perfectly parallel CD. In principle, this picture also applies (with minor differences) to twins and intrinsic pinning.

First, when the angle between the applied field **H** and the correlated defects is smaller than a certain φ_L, it is energetically favorable for the vortices to remain locked into the defects. This is related to the concept of *transverse Meissner effect*. The lock-in angle is

$$\varphi_L \simeq \frac{4\pi\sqrt{2\varepsilon_l\varepsilon_p}}{\Phi_0 H} \tag{2}$$

where ε_l is the vortex line tension. In isotropic superconductors $\varepsilon_l = \varepsilon_0 \ln\kappa$, but in the anisotropic case the situation is rather complex. In our experiments the appropriate line tension is that corresponding to in-plane deformations (see pages 1163-1164 in Ref. 4), $\varepsilon_l = (\varepsilon^2\varepsilon_0/\varepsilon(\Theta))\ln\kappa$, where the mass anisotropy $\varepsilon = m_{ab}/m_c \ll 1$ and $\varepsilon^2(\Theta) = \cos^2(\Theta) + \varepsilon^2\sin^2(\Theta)$. Note that both ε_l and ε_p decrease with T.

For tilt angles larger than φ_L and smaller than a trapping angle, $\varphi_T = \sqrt{2\varepsilon_p/\varepsilon_l}$, vortices form staircases with segments pinned into different defects and connected by unpinned or weakly pinned kinks. Beyond φ_T, vortices become straight lines aligned with the applied field and unaffected by the correlated nature of the pinning potential.

Experimentally, the determination of bulk vortex structures for applied fields tilted with respect to the correlated pinning potential is very difficult. Most of the existing imaging methods that permit direct observation of the vortices can only detect the flux lines at the sample surface[37]. Recent studies have shown that it is possible to resolve individual vortices inside a superconductor with columnar defects by means of Lorentz microscopy[38] or interference microscopy[39]. Unfortunately, however, the low penetration power of the electron beam imposes a strong restriction in the maximum thickness of the sample of about 0.5 μm. Thus, in general, in order to obtain information from the 3D nature of the vortex structure we still have to rely on indirect techniques like dc-magnetization, ac-susceptibility or transport measurements[1, 7, 8, 9, 10, 11, 40, 41, 42, 43, 44]. In this context, it is useful to introduce CD tilted off the crystallographic c axis, as this helps to discriminate the pinning produced by them from that due to twin boundaries and from anisotropy effects.

II. DC MAGNETIZATION: ANGULAR DEPENDENT VORTEX CONFIGURATIONS IN THE SOLID PHASE

A. Introduction to dc-Magnetization Measurements

The widely used dc magnetization measurements are a powerful tool to explore the irreversible response of the vortex system deep into the vortex-solid phases, where electrotransport measurements and ac-susceptibility hardly access. If a superconductor is cooled down in a zero applied field (ZFC experiment) and then an external field $H > H_{c1}$ is applied, flux-bearing vortices enter through the sample's border until their motion is arrested by pinning centers. As a consequence, the system achieves an inhomogeneous flux distribution with a higher density of vortices near the border that progressively decreases toward the center of the sample. The spatial variation of the locally averaged field $\mathbf{B}(\mathbf{r})$ gives rise to supercurrents $\mathbf{J}$ in the sample that, in the stationary state, accommodate to be exactly the critical current J_c everywhere. This is the so-called *Critical State* regime[6, 45].

The simplest version of the critical state is the isotropic Bean model[45], where J_c is assumed to be field independent and isotropic, so the current density throughout the sample (in the fully penetrated state) is necessarily uniform, and the associated irreversible magnetization $\mathbf{M_i}$ is proportional to J_c via a geometrical factor. For instance, for a disk of radius R with $\mathbf{H}$ parallel to its normal $\hat{\mathbf{n}}$ we have $\mathbf{M_i} = (J_c R/3c)\,\hat{\mathbf{n}}$. However, even in this simple case the calculation of the field profile is rather complex, and has been the subject of extensive modelling and numerical analysis[46, 47, 48]. The situation is further complicated when realistic cases of field dependent and anisotropic critical currents are considered[49, 50].

If $\mathbf{H}$ is tilted with respect to $\hat{\mathbf{n}}$, then $\mathbf{M_i}$ has two components, $M_\parallel$ and $M_\perp$, parallel and perpendicular to $\hat{\mathbf{n}}$ respectively (see Fig. 1), that in general depend on the various components of J_c and on the sample geometry. In very thin samples (which is our case), since the non-equilibrium screening currents are constrained to flow parallel to the sample surface, there is a large angular range of applied fields[51, 52] in which $\mathbf{M_i}$ points almost parallel to $\hat{\mathbf{n}}$. For an infinite strip of an isotropic superconductor, Zhukov *et al.*[52] showed that $\mathbf{M_i}$ remains almost locked to $\hat{\mathbf{n}}$ as long as the angle Θ_H between $\mathbf{H}$ and $\hat{\mathbf{n}}$ remains smaller than $\Theta_c = \arctan \nu^{-1}$. Here $\nu = \delta/w$, where δ and w are the thickness and width of the strip respectively, with $\delta \ll w$. For this particular geometry,

$$M_\perp = \frac{\nu}{6c} J_c \tan\Theta_H \quad M_\parallel = \frac{J_c w}{4c}\left(1 - \frac{\nu^2}{3}\tan^2\Theta_H\right) \quad if \quad \Theta_H \leq \Theta_c \tag{3}$$

and the angle Θ_M between $\mathbf{M_i}$ and $\hat{\mathbf{n}}$ is given by,

$$\tan\Theta_M = \frac{M_\perp}{M_\parallel} = \frac{2\nu^2 \tan\Theta_H}{3 - \nu^2\tan^2\Theta_H} \approx \frac{2}{3}\nu^2 \tan\Theta_H \tag{4}$$

Typically we deal with samples of dimensions $\delta \sim 15$ μm and $w \sim 400$ μm, so $\nu \sim 0.04$ and $\Theta_c = 87°$, *i.e.* $M_\parallel \gg M_\perp$ and the geometrical factor changes only 0.1% for $\Theta_H \leq \Theta_c$. On the other hand, for $\Theta_H \geq \Theta_c$ the irreversible moment vector suddenly rotates towards the sample plane.

It must be noted that the total field in the sample results from the applied field plus the *self field* H_{sf} generated by the screening currents. At the center of a thin disk $H_{sf} \sim J_c t$ (rather than $\sim J_c R$) and the shielding currents also create radial fields of $\sim H_{sf}/2$ on the disk surface[46, 47, 48]. For $H < H_{sf}$ self field effects dominate, thus $J_c(H)$ cannot be easily extracted from $M_i(H)$. We constrain our analysis to the regime $H \gg H_{sf}$ in order to obtain reliable estimations using the Bean model. For instance, at $T = 60$ K for YBCO crystals of $\delta \sim 15\mu$m with CD, $J_c \sim 10^5$ A/cm^2 and hence $H_{sf} \sim 150$ G.

In spite of the shortcomings of the Bean model and the necessity of extend this description to account for anisotropies and field dependencies of J_c, several experiments have shown that the behavior of the irreversible magnetization follows accurately this model[53, 54] justifying its use as a reliable way to determine the critical current of the system[55].

The magnetization measurements presented in this section were conducted on a SQUID-based magnetometer Quantum Design MPMS-5S equipped with two sets of detectors, which allows us to record both the longitudinal $M_L(H)$ and the transverse $M_T(H)$ components (parallel and perpendicular to $\mathbf{H}$, respectively) of the total magnetization vector $\mathbf{M}$. The crystals can be rotated *in situ* around an axis perpendicular to $\mathbf{H}$ (see Fig. 1), and they are carefully aligned with the rotating axis normal to the irradiation plane, in such a way that the condition $\mathbf{H} \parallel$ tracks could be achieved within $\sim 1°$.

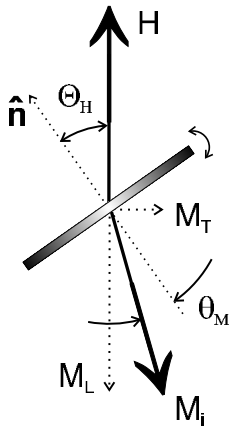

FIG. 1: Sketch showing the orientation of the irreversible magnetization $\mathbf{M_i}$ and applied field $\mathbf{H}$ with respect to the sample normal $\hat{\mathbf{n}}$.

Our usual measurement procedure[56, 57] consists in a ZFC of the sample from above T_c down to the work temperature T at a given Θ_H. Then, both components $M_L(H)$ and $M_T(H)$ of a magnetization loop are recorded (at fixed T and Θ_H). After that, the sample is rotated to a new desired angle, warmed up above T_c and cooled down in zero field to start a new run. The total magnetization vector so obtained is $\mathbf{M} = \mathbf{M_i} + \mathbf{M}_{eq}$, where $\mathbf{M}_{eq}$ is the equilibrium (reversible) magnetization in the mixed state of the superconductor, plus any contribution from the sample holder. We use the widths of the hyterisis $\Delta M_L(H)$ and $\Delta M_T(H)$ to calculate the modulus $M_i = \frac{1}{2}\sqrt{\Delta M_L^2(H) + \Delta M_T^2(H)}$ and the angle $\Theta_M = Atan(\Delta M_T(H)/\Delta M_L(H))$ of $\mathbf{M_i}(\mathbf{H})$. Note that in this way M_{eq} automatically cancels out of the calculation, so it is not necessary to determine it.

We have also developed an alternative method[58] which allows us to obtain directly $M_i(\Theta_H)$ by rotating the sample at fixed H and T. This procedure is much faster, and its principal advantage is that a finer grid can be easily obtained in the angular range of interest, thus permitting the exploration of various regimes with significantly improved angular resolution. The complication is that the M_{eq} is not automatically cancelled, thus it must be subtracted (usually, however, in HTSC the strong pinning determines that $M_i \gg M_{eq}$). We have solved that complication by appropriate data analysis[58], and we have been able to obtain very good agreement between data from sample rotations and from magnetization loops. A rotation at fixed H is to some extent analogous to a hysteresis loop[59]. Rotating the sample normal, $\hat{\mathbf{n}}$, towards $\mathbf{H}$ increases $H_\perp$, which is roughly equivalent to increasing H at $\Theta_H = 0°$, moving along the lower (diamagnetic) branch of the loop. Decreasing $H_\perp$ (either by rotating $\mathbf{n}$ away from $\mathbf{H}$ or by crossing the $\mathbf{H} \parallel \mathbf{c}$ condition), is equivalent to reversing the field sweep, thus producing a switch to the other branch of the loop. This is a useful analogy for the analysis of the rotations, although it should not be pushed too far.

Finally, it is important to mention that, due to the large influence of thermal fluctuations on the vortex dynamics in these HTSC compounds, the persistent current J determined through dc magnetization measurements in the typical time scale of SQUID magnetometers (~ 30 sec.) is much smaller than the "true" critical current density J_c.

B. Angular regimes

1. *Lock-in Phase*

Figure 2 shows typical M_i versus Θ_H curves at $T = 60$ K for a YBCO single crystal with CD at an angle $\Theta_D = 32°$ away from the c axis[56]. As discussed above, the geometrical factor between M_i and J is almost constant for $\Theta_H \leq \Theta_c \sim 87°$ in our crystal, thus the vertical axis in Fig. 2 is directly proportional to the persistent J over almost all the angular range. The uniaxial nature of the pinning potential is clearly manifested as an asymmetric angular response $M_i(\Theta_H) \neq M_i(-\Theta_H)$. At high fields ($H \geq 10$ kOe) we observe a large peak in the direction of the tracks $\Theta_{max} \simeq \Theta_D = 32°$. At lower fields the peak becomes broader and transforms into a plateau (the angular range where $M_i(\Theta_H) \sim const.$) as well as it *progressively shifts away from the tracks in the direction of the c axis* ($\Theta_{max} < \Theta_D$). Hereafter in this section we will focus in the study of the plateau and defer the discussion of the shift to the next section.

The inset of Figure 2 shows a zoom in of the data of the main panel for $H = 4$ kOe, where the plateau is clearly observed. The constancy of $M_i\,(\Theta_H)$ indicates that the pinning

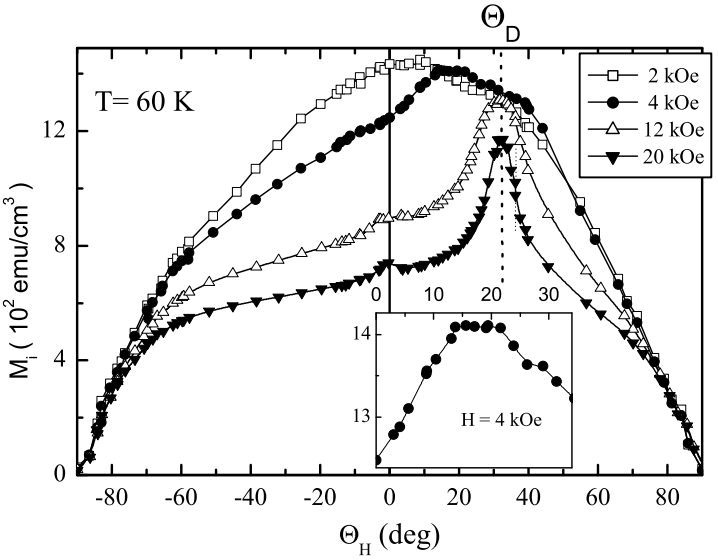

FIG. 2: Irreversible magnetization $M_i(H)$ as a function of Θ_H for several fields, at $T = 60$ K. Inset: zoom in of the data of the main panel for $H = 4$ kOe around the plateau region.

energy remains constant and equal to the value at the alignment condition $\Theta_B = \Theta_D$. This behavior is a fingerprint of the lock-in phase[3]. Moreover, the decrease of M_i at the edges of the plateau is quite sharp, a result consistent with the appearance of kinks, which not only reduce J_c but also produce a faster relaxation. A few examples of the observed plateaus for a $ErBa_2Cu_3O_7$ (ErBCO) single crystal are shown in Figure 3 for several fields and temperatures (some curves have been translated vertically for clarity).

The plateau represents the angular range of applied field over which it is energetically convenient for the vortices to remain locked into the columnar defects, therefore its angular width is twice the lock-in angle φ_L. The results for all measurable plateau widths are plotted as a function of H^{-1} in Figure 4. This figure clearly demonstrates the linear dependence of φ_L on H^{-1} over the whole range of temperature and field of our study (as evidenced by the solid lines which are the best linear fits to the data), in agreement with the Bose-glass prediction [Eq. (2)].

To analyze whether Eq. (2) provides a satisfactory description of the temperature dependence of the lock-in effect, the slopes $\alpha(T) = d\varphi_L/d(H^{-1})$ of the linear fits showed in Fig. 4 are plotted in Fig. 5 (solid symbols). As expected, $\alpha(T)$ decreases with increasing T, reflecting the fact that the lock-in angle at fixed H decreases with T due to the reduction of both, the line tension and the pinning energy. From eqs. (1) and (2) evaluated at the track's direction $\Theta_B = \Theta_D$ we obtain

$$\alpha(T) \approx \frac{\Phi_0 \varepsilon}{8\pi\lambda^2} \ln\left(1 + \frac{r_D^2}{2\xi^2}\right) \times \left[\eta \frac{2\ln\kappa}{\varepsilon(\Theta_D)} f(x)\right]^{1/2}, \qquad (5)$$

where $f(x) \sim \exp(-x)$ for $x > 1$.

We can now fit the experimentally determined $\alpha(T)$ using Eq. (5). To that end we fix the reasonably well known superconducting parameters of the material $\varepsilon \approx 1/5$; $\ln\kappa \approx 4$

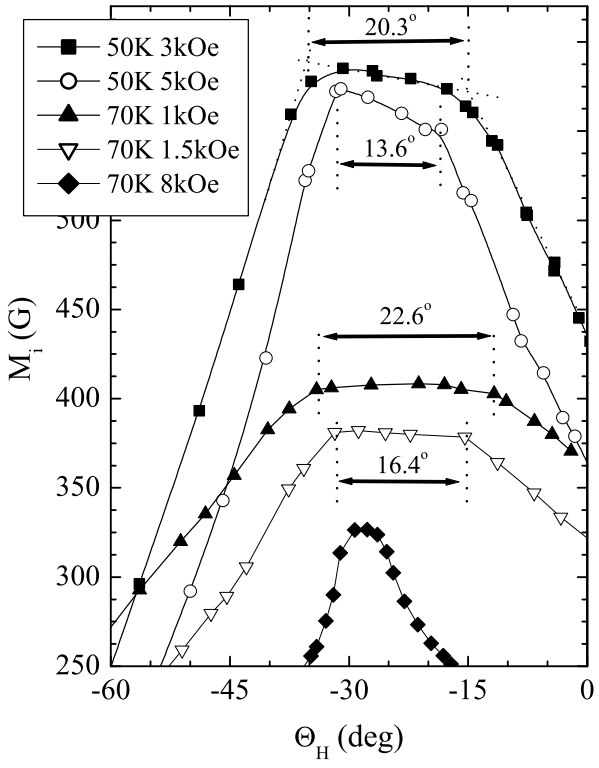

FIG. 3: M_i versus Θ_{max} in the region of the plateau for several fields and temperatures in a ErBCO single crystal.

and $\xi = 15\text{Å}\ /\sqrt{1-t}$ (where $t = T/T_c$). We also assume the usual two-fluid temperature dependence $\lambda(T) = \lambda_L/2\sqrt{1-t^4}$, where λ_L is the zero-temperature London penetration depth. The free parameters are then T_{dp} and the combination $\lambda_L/\eta^{1/4}$. The best fit, shown in Fig. 5 as a solid line, yields $\lambda_L/\eta^{1/4} = 360$ Å and $T_{dp} = 30$ K.

The obtained T_{dp} is smaller, but still reasonably similar to the value ~ 40 K reported for several YBCO crystals using a completely different experimental method[30, 31]. This low T_{dp} (well below the initial theoretical expectations) indicates that the efficiency factor η is rather small, what is also consistent with the less than optimum J_c observed here and in several previous studies. For low matching fields as that used in the present work, it was estimated[30] that $\eta \sim 0.2 - 0.25$.

The exact value of η has little influence in our estimate of λ_L, as it only appears as $\eta^{1/4}$. For $\eta = 0.2$ and $\eta = 1$ we get $\lambda_L = 250$ Å and 360 Å respectively, a factor of 4 to 5 smaller than the accepted value $\lambda_L \sim 1400$ Å. Zhukov *et al.*[11] had reported a similar discrepancy when studying the lock-in effect by both CD and twin boundaries in YBCO. Similarly, as we will show in the next section, we also find that the misalignment between **B** and **H** at low fields can be described satisfactorily using a λ_L smaller than the accepted value[56]. Thus, this numerical discrepancy appears to be a common result associated to the study of angular dependencies in YBCO-type superconductors with correlated disorder that deserves further analysis.

Finally, it is relevant to note that Eq. (2) was derived for the *single vortex pinning*

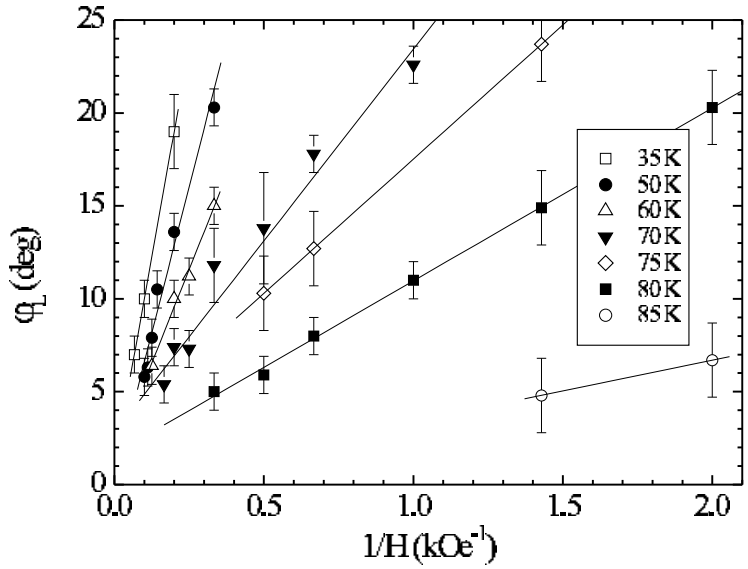

FIG. 4: Plateau widths φ_L vs H^{-1} for several temperatures. The straight lines are fits according to Eq. (2).

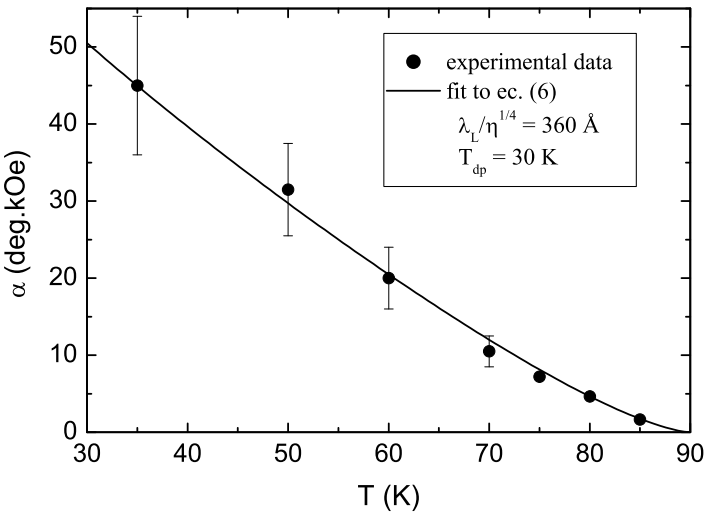

FIG. 5: Slopes $\alpha(T) = d\varphi_L/d(H^{-1})$ of the linear fits of Fig. 4

regime, which occurs below the temperature dependent accommodation field $B_a(T) < B_\Phi$ (section I.C.), while a large fraction of the data shown in Fig. 4 lies above this line, in the *collective pinning* regime. Unfortunately, to our knowledge there is no available expression for $\varphi_L(H,T)$ in the collective regime. Blatter *et al.*[4] only argued that collective effects should result in a reduction of the lock-in angle. The experimental fact is that Eq. (2) satisfactorily describes both the temperature and field dependence of φ_L. This suggests that, at least to a first approximation, collective effects in the range of our measurements

simply result in a different prefactor in Eq. (2).

2. Trapping Angle

As was mentioned in Section I.D., it is expected that for $|\Theta_B - \Theta_D| > \varphi_L$ vortices form staircases. The question that arises here is whether we are able to observe any clue of the trapping angle φ_T from the angular dependence of the irreversible magnetization. For clarity lets concentrate the analysis on high enough fields such that no plateaus or peak shifts appear.

First, we have to notice that for $\Theta_H > \Theta_{\max}$, the asymmetry $M_i(+\Theta_H) > M_i(-\Theta_H)$ in Fig. 2 indicates that pinning is stronger when H is closer to the tracks than in the crystallographically equivalent configuration in the opposite side. This asymmetry demonstrates that at the angle $+\Theta_H$ vortices form staircases, with segments trapped into the tracks. Second, for $\Theta_H < \Theta_{\max}$ we again observe asymmetry, $M_i(\Theta_H)$ crosses $\Theta_H = 0$ with positive slope, indicating that pinning decreases as H is tilted away from the tracks. Thus, we can conclude that staircases extend at least beyond the c axis into the $\Theta_H < 0$ region.

Let's now analyze the topology of the vortex staircases. The angle Θ_k between the kinks and the c axis (see Fig. 6) can be calculated by minimization of the free energy[4]. If L_p is the length of a pinned segment, and L_k the length of the kink, the line energy is $E \propto L_p \epsilon_p(\Theta_D) + L_k \epsilon_f(\Theta_k)$, where $\epsilon_f(\Theta_k) \approx \varepsilon_0 \varepsilon(\Theta_k)[\ln\kappa + 0.5]$ and $\epsilon_p(\Theta_D) \approx \varepsilon_0 \varepsilon(\Theta_D)[\ln\kappa + \alpha_t]$ are the line energy for free and pinned vortices respectively and $\alpha_t < 0.5$ parameterizes the core pinning energy due to the tracks (smaller α_t implies stronger pinning). Minimizing E with respect to Θ_k we obtain the two kink orientations, Θ_k^- for $\Theta_H < \Theta_D$ and Θ_k^+ for $\Theta_H > \Theta_D$.

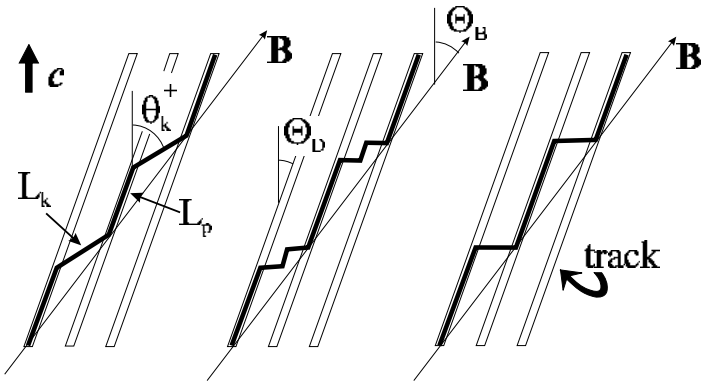

FIG. 6: Sketch showing the possible vortex configurations when the field is tilted with respect to the columnar defects.

Since the tracks are tilted, $\left|\Theta_k^-\right|$ and $\left|\Theta_k^+\right|$ are different. However, those angles are independent of Θ_H. As $|\Theta_H - \Theta_D|$ increases, $\Theta_k^\pm$ remain constant while L_p decreases and the number of kinks increases, consequently the pinning energy lowers. This accounts for a decreasing M_i as $\mathbf{H}$ is tilted away from the tracks. In particular, for $\Theta_H = \Theta_k^\pm$ vortices become straight ($L_p = 0$), thus $\varphi_T^\pm = \left|\Theta_k^\pm - \Theta_D\right|$ are the trapping angles in both directions. In general $\Theta_k^\pm$ must be obtained numerically, but for $\varepsilon \tan\Theta_k \ll 1$ and $\varepsilon \tan\Theta_D \ll 1$ we obtain

$$\tan\Theta_k^{\pm} \approx \tan\Theta_D \pm \frac{1}{\varepsilon}\sqrt{\frac{1-2\alpha_t}{\ln\kappa + 0.5}} \tag{6}$$

Eq.(6) adequately describes the main features of the asymmetric region[56, 60] in Fig. 2, and for $\Theta_D = 0$ it coincides with the usual estimates[3, 4] of φ_T. There is, however, an important missing ingredient in the standard description presented above, namely the existence of twins and Cu-O layers, which are additional sources of correlated pinning. This raises the possibility that vortices may simultaneously adjust to more than one of them, forming different types of staircases (see Fig. 6).

Pinning by twin boundaries is visible in Figure 2 as an additional peak centered at the c axis for $H = 20$ kOe. A zoom in of that peak is shown in Figure 7. The width of this peak, $\sim 10^{\circ}$, is in the typical range of reported trapping angles for twins[7, 8, 9, 10, 11]. The fact that the peak is mounted over an inclined background implies that vortices are also trapped by the tracks. Thus, vortices in this angular range contain segments both in the tracks and in the twins. These two types of segments are enough to build up the staircases for $\Theta_H > 0$, but for $\Theta_H < 0$ a third group of inclined kinks with $\Theta_k < 0$ must exist in order to have vortices parallel to **H** (see sketches in Fig. 7).

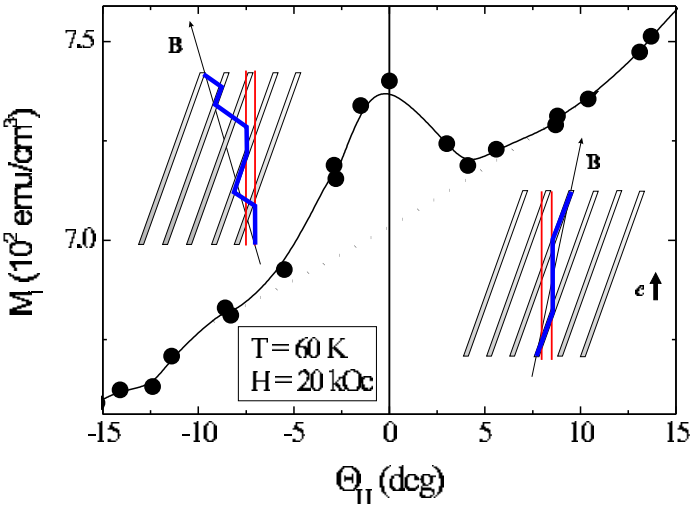

FIG. 7: Zoom in of the data shown in Fig. 2 for $H = 20$kOe around the c axis. The sketches represent vortex staircases for $\Theta_H > 0$ and $\Theta_H < 0$.

Another fact to be considered is that the asymmetry in $M_i(\Theta_H)$ disappears as Θ_H approaches the ab planes. This is illustrated in Figure 8, where M_i data for $-|\Theta_H|$ was reflected along the c axis and superimposed to the results for $+|\Theta_H|$. There is a well defined angle Θ_{sym} beyond which $M_i(\Theta_H)$ recovers the symmetry with respect to the c axis (see inset in Figure 8).

One possible interpretation is that for $\Theta_H > \Theta_{sym}$ staircases disappear, *i.e.* $\Theta_{sym} = \Theta_k^+$, and we are determining the trapping angle $\varphi_T^+ = \Theta_{sym} - \Theta_D$. However, this is inconsistent with our experimental results. Indeed, φ_T^+ should decrease with T, and this decrease should be particularly strong above the depinning temperature $T_{dp} \sim 30-40$ K due to the reduction

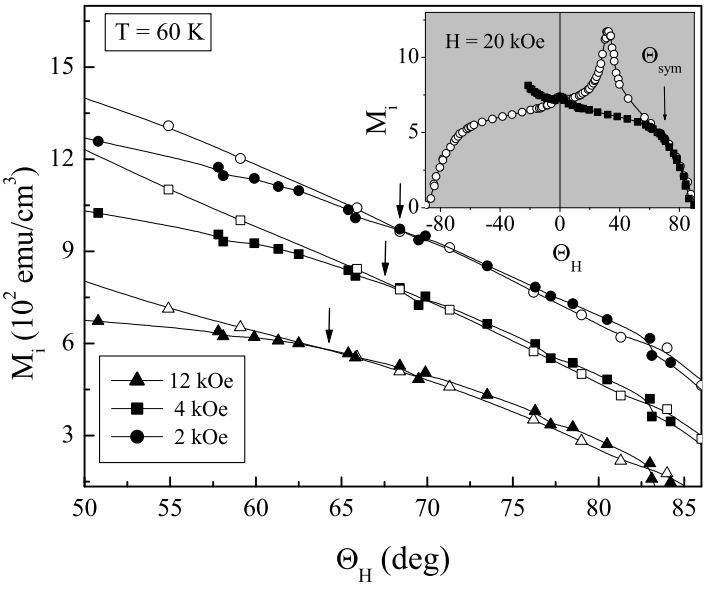

FIG. 8: Angular dependence of the irreversible magnetization M_i for three different fields at $T = 60$ K. Open symbols: data for $\Theta_H > 0$. Solid symbols: data for $\Theta_H < 0$, reflected with respect to the c axis. Some of the curves were shifted vertically for clarity. The arrows indicate the angle Θ_{sym} beyond which the behavior is symmetric with respect to the c axis. The procedure of reflection of the data is shown in the inset.

of the pinning energy by entropic smearing effects (section I.C). This expectation is in sharp contrast with the observed increase of Θ_{sym} with temperature, which is shown in Figure 9 for $H = 2$ T. Thus, the interpretation of Θ_{sym} as a measure of the trapping angle is ruled out. Moreover, if in a certain angular range vortices were not forming staircases, pinning could be described by a scalar disorder strength, then at high fields $M_i(\Theta_H)$ should follow the anisotropy scaling law[61] $M_i(H, \Theta_H) = M_i(\varepsilon(\Theta_H) H)$. Consistently, we do not observe such scaling in any angular range[62].

Our alternative interpretation is that, as **H** approaches the *ab* planes, the kinks become trapped by the intrinsic pinning. This idea has been used by Hardy *et al.*[43] to explain that the J_c at low T in the very anisotropic Bi and Tl compounds with tracks at $\Theta_D = 45°$ was the same for H either parallel or normal to them. Our situation is somewhat different, as we are comparing two configurations both having kinks.

We first note that, according to Eq. (6), $\Theta_k^{\pm}$ cannot be exactly 90° for finite ε, thus the intrinsic pinning must be incorporated into the model by assigning a lower energy to kinks exactly parallel to the *ab* planes. Vortices may now form structures consisting of segments trapped in the columns connected by segments trapped in the *ab* planes, or alternatively an inclined kink may transform into a staircase of smaller kinks connecting segments in the planes (see Fig. 6). We should now compare the energy of the new configurations with that containing kinks at angles $\Theta_k^{\pm}$. This is equivalent to figure out whether the kinks at $\Theta_k^{\pm}$ lay within the trapping regime for the planes or not. The problem with this analysis is that, as $\Theta_k^{\pm}$ are independent of Θ_H, one of the two possibilities (either inclined or trapped kinks), will be the most favorable for all Θ_H. Thus, this picture alone cannot explain the crossover

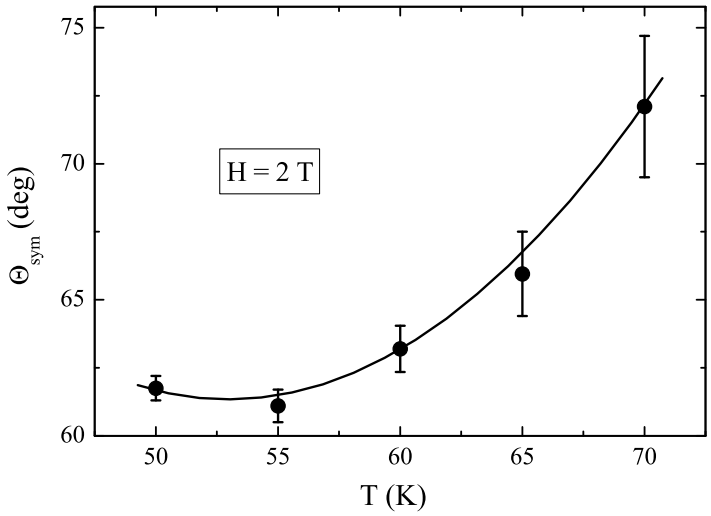

FIG. 9: Temperature dependence of Θ_{sym} defined using the criterium showed in Fig. 8. The solid line is a guide to the eye.

from an asymmetric to a symmetric regime in $M_i\,(\Theta_H)$.

The key concept to be considered in this scenario is the dispersion in the pinning energy of the tracks[3, 4]. The angles $\Theta_k^{\pm}$ depend on the pinning strength of the adjacent tracks (α_t in Eq. (6)), thus a dispersion in α_t implies a dispersion in $\Theta_k^{\pm}$. As Θ_H increases, it becomes larger than the smaller $\Theta_k^{\pm}$'s (that connect the weaker defects) and the corresponding kinks disappear. The vortices involved, however, do not become straight, but remain trapped by stronger pins connected by longer kinks with larger $\Theta_k^{\pm}$. This process goes on as Θ_H grows: the weaker tracks progressively become ineffective as the "local" Θ_k is exceeded, and the distribution of $\Theta_k^{\pm}$ shifts towards the *ab* planes. When a particular kink falls within the trapping angle of the planes, a switch to the pinned-kink structure occurs. In this new picture, the gradual crossover to the symmetric regime as $|\Theta_H|$ increases takes place when most of the remaining kinks are pinned by the planes.

If kinks become locked, the total length of a vortex that is trapped inside columnar defects is the total length of a track, independent of Θ_H, and the total length of the kinks is $\propto |\tan\Theta_H - \tan\Theta_D|$. As $|\Theta_H|$ grows, the relative difference between the line energy in both orientations decreases, an effect that is reinforced by the small line energy of the kinks in the *ab* planes. If kinks are not locked but rather form staircases, taking into account that the trapping angle for the *ab* planes is small[8], the same argument still applies to a good approximation. The temperature dependence of Θ_{sym} is now easily explained by a faster decrease of the pinning of the *ab* planes with T as compared to the columnar defects.

Additional evidence in support of our description comes from transport measurements in the dc-flux transformer configuration where, in the liquid phase in *twinned* YBCO crystals (without CD) vortices remain correlated along the c axis *for all field orientations*[63], in contrast to the observed behavior in untwinned crystals. This suggest that, for all angles, vortices are composed of segments in the twins and in the *ab* planes.

C. Influence of the Material Anisotropy and Sample Geometry

In the previous section we showed that the presence of columnar defects in HTSC increases the critical current due to the strong pinning and the reduced vortex wandering when flux lines are trapped into the pinning potential. We have also shown that at high fields, $J_c(\Theta_H)$ exhibits a peak when the applied field is aligned with the tracks orientation. As field decreases, two distinct phenomena progressively and simultaneously appear. On one hand, we observe a plateau which reflects the existence of a lock-in phase. On the other hand, we noticed that the peak shifts towards the c axis. In this section we present a throughout study of the origin of this displacement and demonstrate that this shift is a consequence of the misalignment between the external and internal field owing to the competition between anisotropy and geometry effects.

1. Relationship between Internal and Applied Fields

In thermodynamic equilibrium, the internal field $\mathbf{B}$ is determined by minimization of the free energy[4] $G(\mathbf{B}) = F(\mathbf{B}) - \frac{B^2}{8\pi} + \frac{(\mathbf{B}-\mathbf{H})\mathbf{M}}{2}$, where $\mathbf{H} = \mathbf{B} - 4\pi(1-\hat{\nu})\mathbf{M}$. The components of the demagnetization tensor $\hat{\nu}$ at the sample principal axes are (ν_x, ν_y, ν_z), with $\nu_x + \nu_y + \nu_z = 1$. We adopt the notation that z coincides with the crystallographic c axis, and that the x axis is perpendicular to both c and $\mathbf{H}$. By standard minimization of $G(\mathbf{B})$ with respect to B_y and B_z, and using the free energy $F(\mathbf{B})$ for the intermediate fields regime ($H_{c1} \ll H \ll H_{c2}$) we obtain,

$$sin(\Theta_B - \Theta_H) = -\frac{f(\nu_y, \nu_z, \varepsilon)\sin(2\Theta_B)}{8\kappa^2}\frac{\ln h + 1}{h} \tag{7}$$

where $f(\nu_y, \nu_z, \varepsilon) = (1-\nu_z) - (1-\nu_y)\varepsilon^2$, Θ_B is the direction of the internal field, and the reduced field $h = H/H_{c2}(\Theta_B, T)$.

The result (7) only assumes uniaxial anisotropy and the coincidence of one principal axis with the c axis, and it shows that under those very general conditions the misalignments due to both mass anisotropy and sample geometry *have the same field and temperature dependence*. The function $f(\hat{\nu}, \varepsilon)$, which contains the combined effects of geometry and anisotropy, is the key ingredient of the low field behavior, as its sign determines whether Θ_B leads or lag behind Θ_H.

To be more specific, let's consider the typical platelike shape of all the studied single crystals, with thickness δ along the c axis much smaller than the lateral dimensions L_x and L_y. To a first approximation $\nu_x = \delta/L_x$ and $\nu_y = \delta/L_y$, thus $\nu_x, \nu_y, (1-\nu_z) \ll 1$. If the material is strongly anisotropic and the crystal is not too thin, then $(1-\nu_z) > (1-\nu_y)\varepsilon^2$, thus $f > 0$ and $\Theta_B > \Theta_H$. We will call this the "anisotropy-dominated" situation. In contrast, for thin enough samples of a not too anisotropic material $(1-\nu_z) < (1-\nu_y)\varepsilon^2$, so $\Theta_B < \Theta_H$. This is what we will call the "geometry-dominated" case. The extreme limit of this case, with an infinite slab ($\nu_x = \nu_y = 0$) and ignoring the anisotropy, has been discussed by Klein *et al.*[41]. It is also worth to note that for an infinite cylinder with axis perpendicular to $\mathbf{H}$, where the geometry effects are expected to cancel out, $\nu_x = 0$ and $\nu_y = \nu_z = \frac{1}{2}$, thus $f \propto (1-\varepsilon^2)$ and Eq. (7) reduces to the well known expression for the bulk[4, 56].

The Eq. (7) allows us to determine which should be the vortex direction Θ_B for a given angle Θ_H of the controlled variable $\mathbf{H}$. In other words, we might use the columnar defects

as detectors of the internal field orientation taking profit from the fact that J_c maximizes when $\Theta_B = \Theta_D$. Thus, if we know Θ_D and Θ_{max}, we are able to determine the misalignment $\Theta_B - \Theta_H = \Theta_D - \Theta_{max}$. Although the *sign* of such misalignment is solely determined by the sign of f, its *magnitude* also depends on additional factors such as $\sin(2\Theta_D)$ and κ^2. Besides that, the misalignment is strongly temperature and field dependent. It is easy to see from Eq. (7) that $\Theta_B \to \Theta_H$ for large enough h.

At this point it is important to note that, although the misalignment between **B** and **H** is a low field effect, Eq. (7) can only be used for $H \gg H_{c1}$. It turns out that all our data are well described by eq. (7). However, the very dilute vortex limit is conceptually interesting, and a detailed discussion about it can be found in Ref. 64.

Table I summarizes the information about geometrical dimensions, mass anisotropy, dose-equivalent matching field B_Φ and angle Θ_D of the CD with respect to the c axis, for all the crystals that we will refer in this section.

TABLE I: Irradiation and shape specifications for all the crystals studied in this section. Crystal B was grown at the T.J. Watson Research Center of IBM and irradiated at the Holifield accelerator, Oak Ridge (USA) with 580 MeV Sn^{30+}.

Crystal	material	ε^{-1}	$B_\Phi(kOe)$	Θ_D	$\delta(\mu m)$	$L_y(\mu m)$	$L_x(\mu m)$	$\nu_y(\times 10^{-3})$	$\nu_x(\times 10^{-3})$	$f(\hat{\nu},\varepsilon)(\times 10^{-3})$
A	$YBa_2Cu_3O_7$	7	30	32°	8.5	210	630	40	13.5	+34
B	$YBa_2Cu_3O_7$	7	30	30°	20.9	715	2150	29	9.7	+19
C	$YBa_2Cu_3O_7$	7	57	30°	11.5	1050	1050	11	11	+1.8
D	$YBa_2Cu_3O_7$	7	22	57°	4.3	381	762	11.3	5.6	-3.2
E	$NbSe_2$	3	0.5	27°	7.7	765	640	10.1	12	-67
F	$NbSe_2$	3	0.5	27°	7.7	585	640	13.2	12	-63.5
G	$NbSe_2$	3	0.5	27°	7.7	419	640	18.4	12	-58

2. Anisotropy-dominated case

In Fig. 2 we have already shown the data corresponding to sample A where we noticed that the maximum in J_c moves towards the c axis as H decreases. As shown in Fig. 10, this effect persist at $T = 70$ K. A similar behavior is observed in crystal B (see Fig. 10), although the shift turns out to be smaller than in A at $T = 70$ K. These two crystals have the same anisotropy and irradiation conditions, but different shapes. Thus, at the same T and H all factors in Eq. (7) are identical, except for $f(\hat{\nu},\varepsilon)$. As seen in Table I, the difference in demagnetizing factors results in a smaller $f(\hat{\nu},\varepsilon)$ for sample B than for A. Hence, the misalignment in sample B is expected to be smaller, as indeed observed.

3. Compensated case

A striking result predicted by Eq. (7) is that the competing effects (anisotropy and geometry) could be exactly compensated if one were able to tune the demagnetizing factors and the anisotropy in order to get $f(\hat{\nu},\varepsilon) = 0$, a condition that is satisfied for $1 - \nu_z = (1 - \nu_y)\,\varepsilon^2$. For the YBCO single crystals, $\varepsilon \sim 1/7$, and this requires extremely thin samples with a big area. Table I shows that crystals C and D almost satisfy this compensating condition, as the absolute values of their $f(\hat{\nu},\varepsilon)$ are, respectively, a factor of ~ 20 and ~ 10 smaller than in A. The right panel of Fig. 10 shows the angular dependence of M_i for these

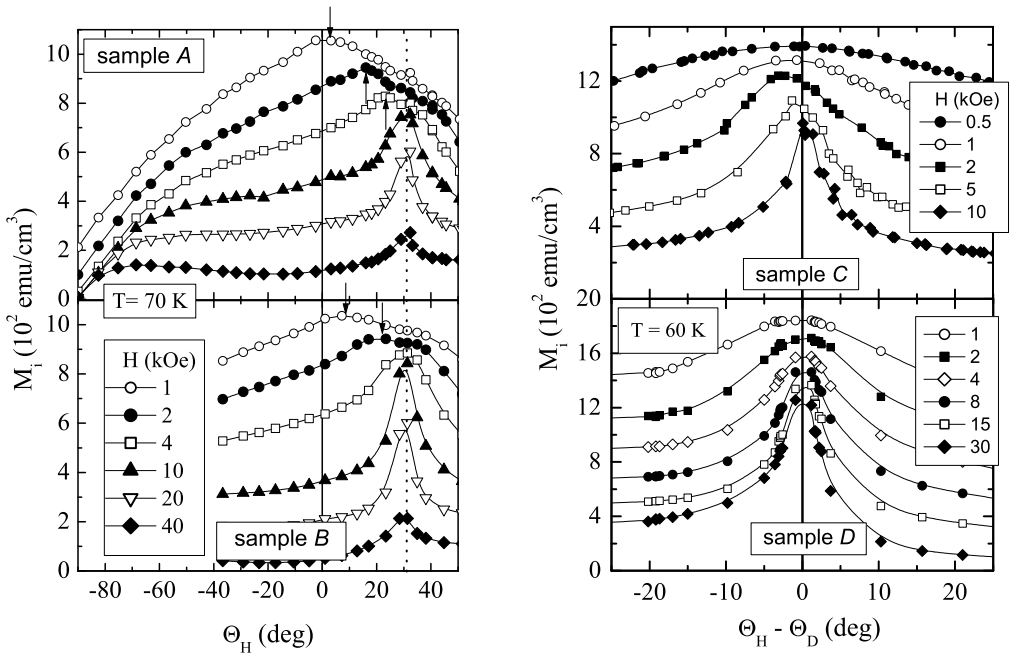

FIG. 10: Left panel: angular dependence of the irreversible magnetization for several fields at $T = 70$ K for the samples A and B (YBCO). The arrows indicate the angular position, Θ_{max}, of the maximum in $M_i(\Theta_H)$ for the lowest fields. Right panel: irreversible magnetization as a function of the relative angle $\Theta_H - \Theta_D$ for several fields at $T = 60$ K in samples C and D (YBCO). For clarity, some curves have been translated vertically.

two crystals at $T = 60$ K. Since the CD orientations Θ_D in samples C and D are different, in order to compare them we set the abscise as the relative angle $\Theta_H - \Theta_D$. In this figure we clearly observe that the peaks remain locked at the tracks direction even for the lowest fields, in complete agreement with the expectation. The same behavior was observed for other temperatures.

4. Geometry-dominated case

So far, the samples studied were YBCO crystals with the same anisotropy but different geometries. On these samples we observed that the peak either shifts in the direction of the c axis or almost does not deviate from the CD direction. As pointed out previously, this behavior arises from the strong anisotropy effect in this material. In order to change the sign of the deviation (*i.e.*, a shift toward the *ab* plane), we need to reduce the anisotropy effects. (Table I shows that crystal D has $f < 0$, thus strictly speaking it is in the geometry-dominated case, but the shift is too small to be detected).

To that end we decided to measure $NbSe_2$ single crystals, which have $\varepsilon \sim 1/3$, making the anisotropy effect about 5 times smaller than in YBCO. Beside this, very large and thin

$NbSe_2$ crystals can be readily found, and they can be tailored at will to obtain the desired shape. Thus, we irradiated a rectangular crystal (labelled as sample E), such that it is in the extreme geometry-dominated case, with $f(\hat{\nu},\varepsilon) \ll 0$. Fig. 11(a) shows $M_i(\Theta_H)$ for this sample at $T = 4.4$ K for several H. At high fields we observe a peak at the tracks' direction $\Theta_D = 27°$. As field decreases the peak becomes broader and, in contrast to the YBCO behavior, it progressively moves away from Θ_D toward the ab plane, in agreement with a negative $f(\hat{\nu},\varepsilon)$.

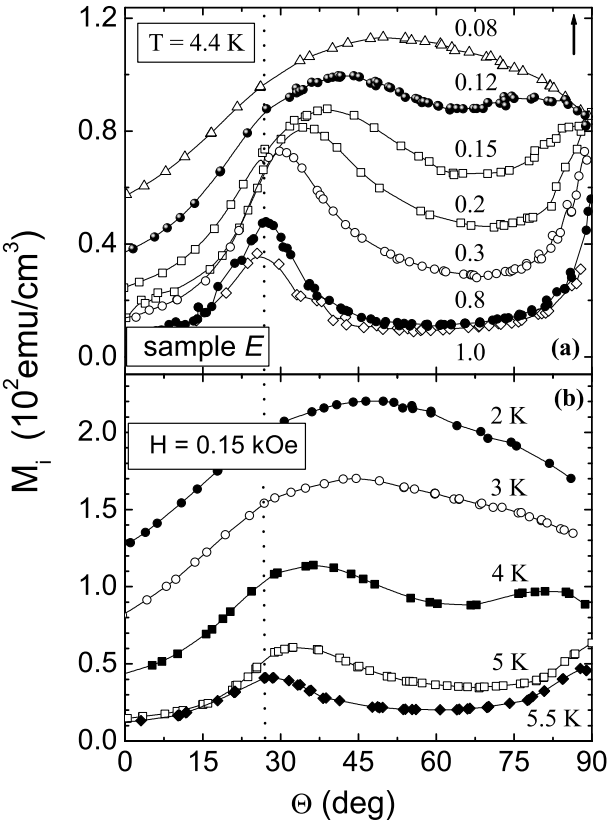

FIG. 11: Angular dependence of the irreversible magnetization for sample E ($NbSe_2$) at (a) $T = 4.4$ K for several fields (in units of kOe), (b) $H = 0.15$ kOe for several temperatures.

The conclusive evidence that the function $f(\hat{\nu},\varepsilon)$ dominates the behavior of the misalignment $\Theta_B - \Theta_H$ comes from samples F and G, which are pieces of crystal E. These samples were obtained by cutting the sample E along a line parallel to its shortest side, in such a way that the demagnetizing factor ν_x remains unaltered, but ν_y increases. In this way, the absolute value of the function $f(\hat{\nu},\varepsilon)$ was progressively reduced, *i.e.*, we moved away from the "extreme geometry-dominated case" and approached the "compensated case" (see Table I). According to Eq. (7), the deviation of the maximum in $M_i(\Theta_H)$ for given H and T should become progressively smaller for crystals F and G as compared to crystal E. This is in fact observed, as demonstrated in Fig. 12, where $\Theta_{max} - \Theta_D$ for crystals E, F and G is plotted as a function of $h = H/H_{c2}(T,\Theta_H)$.

The misalignments for all the YBCO crystals shown in Figs. 2 and 10 are also included in Fig. 12. Thus, this figure summarizes all the samples studied in the present work, at

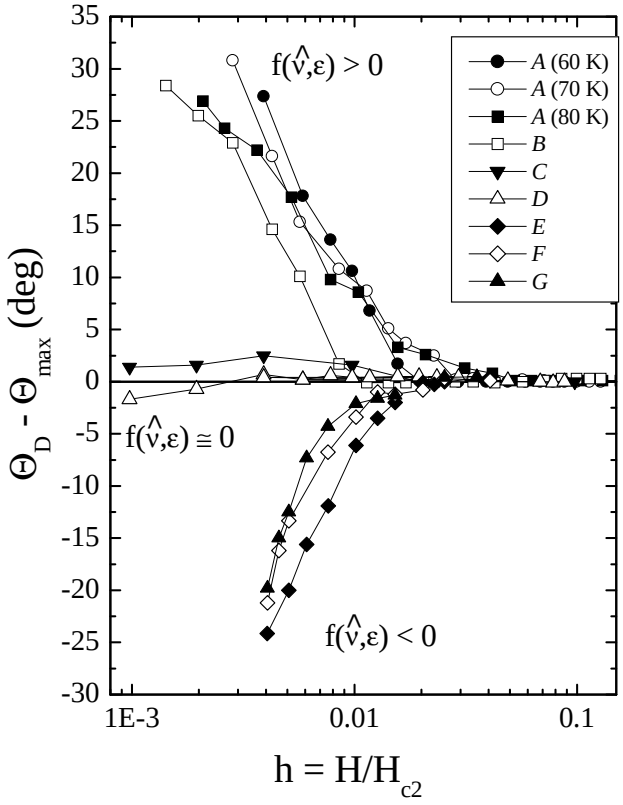

FIG. 12: Deviation in the maximum of the irreversible magnetization with respect to the tracks' direction $\Theta_D - \Theta_{max}$, as a function of $h = H/H_{c2}$, for all samples studied in the present work.

various temperatures and fields. The three possible low field behaviors are clearly visible: anisotropy-dominated (upward curvature), geometry-dominated (downward curvature) and compensated (almost horizontal curves). It is worth to note that, in all the not-compensated cases and for both materials, the misalignment between **B** and **H** becomes relevant for fields below a certain characteristic field $H \sim 0.02 H_{c2}$.

5. Quantitative test of the model

The above results clearly demonstrate that the qualitative differences in the low field behavior are controlled by the factor $f(\hat{\nu}, \varepsilon)$. We now want to verify whether the H and T dependence of the shift is well described by the model. According to Eq. (7) these two variables appear only through the combination $h = H/H_{c2}(\Theta_B, T)$. Thus, $|\Theta_D - \Theta_{max}|$ should increase not only with decreasing H at fixed T, as already seen in figs. 10 and 11(a), but also with decreasing T at fixed H, due to the increase in $H_{c2}(T)$. This second expectation is also verified, as shown in Fig. 11(b) where $M_i(\Theta_H)$ for sample E was plotted at constant field $H = 0.15$ kOe for several temperatures.

The equivalence between the variations in T and H is quantitatively verified in Fig. 13, where $\sin(\Theta_{max} - \Theta_D)/f(\hat{\nu}, \varepsilon)$ is plotted as a function of h for the two sets of data shown in Fig. 11(a) and 11(b). We observe a good scaling, thus confirming that h is the appropriate variable. The upper critical field values $H_{c2} = 51.8$ kG$(1 - t)$ were taken from the literature [65], thus the superposition of the two curves involves no free parameters.

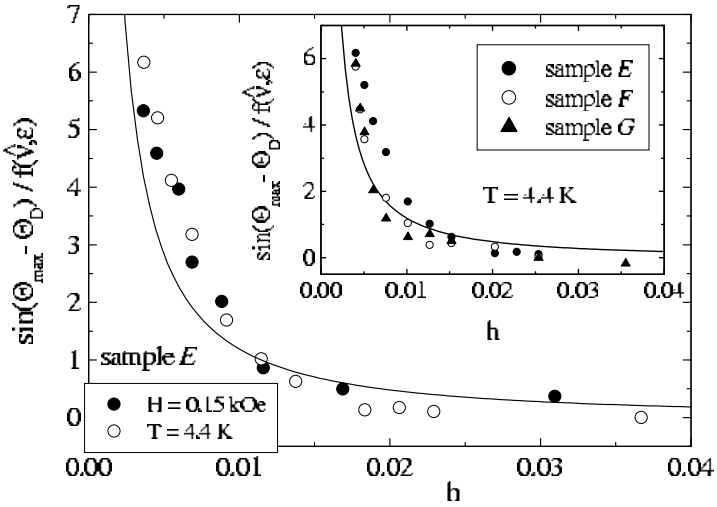

FIG. 13: Main panel: $\sin(\Theta_{max} - \Theta_D)/f(\hat{\nu}, \varepsilon)$ vs h for the two sets of data shown in Fig. 11(a) and 11(b) for the sample E. Solid symbols: H fixed and T swept. Open symbols: T fixed and H swept. Inset: the same scaling shown in the main panel for samples E, F and G. The solid line in both, main panel and inset, corresponds to Eq. (7) with $\Theta_B = \Theta_D = 27^\circ$ and $\kappa = 5.6$.

Finally, we analyze the quantitative effect of the factor $f(\hat{\nu}, \epsilon)$. This factor is a constant for a given sample, so it is the same for all the data in the main panel of Fig. 13. In contrast, in the inset we show the same scaling procedure for the crystals E, F and G at $T = 4.4$ K, so now $f(\hat{\nu}, \epsilon)$ is different for each sample, while all the other parameters remain identical. We again obtain a good superposition of the data, although the scaling is poorer than in the main panel, probably due to the damage produced in the crystal after each cut process.

The solid line in the main panel of Fig. 13 depicts the expectation of Eq. (7), with $\Theta_B = \Theta_D = 27^\circ$ as experimentally determined from the location of the maximum at high fields, and a single fitting parameter $\kappa = 5.6$. The same curve is shown in the inset. The value $\kappa = 5.6$ is smaller than the accepted value[65] $\kappa \sim 9$, a similar discrepancy to that observed when studying the lock-in effect.

6. The Role of the Columnar Defects

It is important to keep in mind that the shift in Θ_{max} at low h is *not* due to the CD. We are only using them as a passive non perturbative tool to measure the vortex direction in the bulk of the samples, what is not easy to do by other methods. In fact, the pinning of the CD is not contained in Eq. (7), which arises from the minimization of a free energy, and thus describes a state of thermodynamic equilibrium. It is obvious, on the other hand, that the uniaxial pinning of these correlated structures is relevant and should be included

in the analysis. This is usually done by adding to the free energy a term F_{pin} that accounts for the correction to the vortex self-energy due to the CD, and then comparing the energy of alternative configurations[4, 43].

This additional contribution depends on the orientation of the vortices, $F_{pin} = F_{pin}(\Theta_B)$, and it is always negative, reflecting the fact that, for $\Theta_B \neq \Theta_D$, the CD promote the formation of staircase vortices whose self energy is lower than that of a straight vortex at the same average orientation. $F_{pin}(\Theta_B)$ decreases as Θ_B approaches Θ_D due to the increase of the core trapped fraction, and it minimizes for that orientation, when the vortex cores are totally trapped into the tracks[4]. The key point in the context of the present study, however, is that the incorporation of $F_{pin}(\Theta_B)$ into the scenario does not modify the previous results, as we show below.

Let's first consider that **H** is applied at the angle $\Theta_H = \Theta_{max}$ such that, in the absence of pinning and according to Eq. (7), the vortices would be at the angle $\Theta_B = \Theta_D$. If we now "turn on" $F_{pin}(\Theta_B)$, the only effect will be to deepen the already existing minimum of the free energy at this orientation, without changing the angle.

Let's now suppose that **H** is applied at an angle Θ_H slightly smaller or slightly larger than Θ_{max}. In the absence of pinning vortices would respectively orient at angles Θ_B slightly smaller or slightly larger than Θ_D, according to Eq. (7). The addition of the term $F_{pin}(\Theta_B)$ will now shift the vortices towards Θ_D, that is, a kind of effective *angular attractive potential* towards the CD orientation will develop. In particular, for $|\Theta_H - \Theta_{max}| < \varphi_L$, the influence of $F_{pin}(\Theta_B)$ will be so strong that the system will minimize its free energy by orienting the vortices exactly along the CD. In section II.B. we have extensively studied this effect, that manifests in our measurements as a *plateau* in $M_i(\Theta_H)$ of width $2\varphi_L$. Note that the center of the plateau coincides with Θ_{max}. Thus, although the relation Θ_B vs Θ_H will be modified by the CD, the angle Θ_{max}, experimentally defined as the maximum in $M_i(\Theta_H)$ or as the center of the plateau where necessary, will still be given by Eq. (7).

III. AC RESPONSE: DYNAMICS REGIMES WITH COLUMNAR DEFECTS NEAR THE SOLID-LIQUID TRANSITION.

In the previous section we have used dc magnetization measurements to identify and characterize vortex structures at different orientations deep in the vortex-solid phase, that is, well below the irreversibility line. What changes in this picture if we increase T and get very close to $H_{irr}(T)$? A first issue is that both the vortex characteristic energy ε_0 and the effective pinning energy ε_p decrease (the last one particularly fast due to the entropic factor), so the lock-in angle φ_L tends to zero. As $H_{c2}(T)$ also decreases, the misalignment effects described in II.C, which are proportional to H_{c2}/H (see Eq. (7)), also diminish. Thus, (except perhaps at extremely low fields) we expect a sharp peak in J_c at the angle Θ_D. A point that is far less obvious is whether staircases will still form for all orientations, what is their structure, and whether the various correlated pinning mechanisms will remain coupled.

Of course $J_c(T) \propto \varepsilon_p$ tends to vanish (for any orientation of **H**) as we approach H_{irr}, thus magnetization measurements are not sensitive enough to explore this regime. So we will now turn our attention to the ac susceptibility, which has also been extensively used to explore the vortex dynamics in HTSC with both correlated an uncorrelated disorder. Indeed, this is a natural complement of the dc magnetization studies. The broad range of amplitudes and frequencies of the ac field easily accessible with this technique allows the exploration

of the dynamics of the vortex system not only in the critical state but in a variety of other dynamic regimes.

When comparing both types of studies, a key factor to be taken into account is the characteristic size of the vortex displacements involved. When measuring magnetization loops, the field changes produce vortex displacements much larger than the distance between defects. The excitations explored by creep measurements, on the other hand, are *half loops*, *double kinks* and *superkinks* (see section I.C.), which expand until the vortex (or bundle) is completely removed from the CD. So all these measurements involve vortex motion through the pinning landscape at an *inter-valley* scale. In contrast, ac susceptibility measurements can be carried out at ac field amplitudes so small that pinned vortices only perform transverse oscillations that are uniform along the field direction and whose amplitude is only a fraction of the pinning range of a columnar defect, *i.e.*, *intra-valley* motion. This particularly interesting situation, which results in a linear response with a very scarce dissipation, allows to sense the curvature of the pinning potential wells [6, 66].

In this section we will use ac susceptibility as a tool to first investigate the angular regimes that exist in the vortex system in the presence of CD in the vicinity of the solid-liquid boundary, and then to explore the dynamic behavior of those regimes in a wide range of current densities and excitation frequencies. We construct the dynamic phase diagram of the system in the temperature vs. ac magnetic field plane and we determine the various crossover fields and currents, as well as the parameters that characterize the different pinning regimes. To achieve that, we have developed a couple of useful procedures for the analysis of the data. It will become apparent that the characterization of the dynamic regimes is essential for the correct interpretation of the angular dependence in the ac response.

A. Experimental technique

To measure the complex AC susceptibility $\chi = \chi' + i\chi"$, crystals were fixed to one coil of a compensated secondary pair rigidly built up inside a long primary coil that produces an ac field $h_a e^{i\omega t}\hat{\mathbf{n}}$ which is parallel to the c axis and is very homogeneous in the volume occupied by the sample. The amplitude h_a can be varied from 5 mOe to 8 Oe and the frequency $f = \omega/2\pi$ from 300 Hz to 100 kHz. A uniform static field $\mathbf{H_{dc}}$ up to 1300 Oe is added. The AC coils setup and the sample can be rotated with a precision of $\sim 1°$, allowing to vary the angle Θ between the c axis and $\mathbf{H_{dc}}$. (Notation: At the high temperature, near T_{BG}, where these measurements are performed, we can consider $\mathbf{B} \parallel \mathbf{H}$. Thus, throughout this section we will refer simply to the angle Θ between the DC field and the c axis, $\Theta = \Theta_H = \Theta_B$. We also refer to the angle $\varphi = \Theta - \Theta_D$ between $\mathbf{H_{dc}}$ and the tracks.)

Measurements are performed in all the cases by slowly warming up the sample. Generally, several curves at various amplitudes h_a or at different angles Θ were recorded during each temperature sweep. The scan in angle was always performed in the same direction to avoid backlash problems. All the curves of χ' and $\chi"$ at each frequency are normalized by the same factor, corresponding to a total step $\Delta\chi' = 1$ with $H_{dc} = 0$. We carefully looked for and confirmed the absence of thermal decoupling between sample and thermometer, as well as measurable heating effects due to the excitation current in the primary coil at high amplitudes.

In each sample, we define the critical temperature T_c as the onset of the AC transition at $H_{dc} = 0$ in the linear AC regime (very low h_a), and the zero field transition width ΔT_c as

the range with nonzero dissipation in the same condition. The low irradiation doses applied in all the samples reported in this section, produce no measurable effect either in the critical temperature or in the transition width.

B. Angular dependence of the ac response.

In this section we will identify several angular ranges where pinning is dominated by different mechanisms. With this scope, we will compare the overall angular response of irradiated and virgin samples. We present measurements performed on two twinned $YBa_2Cu_3O_7$ single crystals from the same batch, both having the same $T_c = 91.8$ K and $\Delta T_c \simeq 0.6$ K. One of them (sample A) was irradiated at room temperature with 291 MeV Au^{27+}ions with a dose-equivalent matching field $B_\phi \sim 700$ Oe at an angle $\Theta_D = 30^o$ from the c axis, and the other one (sample B) was used as a reference.

Figures 14(a) and 14(b) show some of the experimental χ' curves recorded as a function of temperature with $H_{dc} = 360$ Oe at different angles Θ in both the virgin and irradiated crystals. The zero field transitions are also included as a reference. Comparison of both figures shows that when the direction of $\mathbf{H_{dc}}$ is close to the ab planes (curves for $\Theta = 92°$ in Fig. 14(a) and $\Theta = 91°$ in Fig. 14(b), shown with solid squares) the response of both samples is very similar, indicating that the pinning properties in that configuration are not significantly altered by the introduction of CD. In contrast, at all other field orientations the irradiation produces a clearly visible upward shift of the $\chi'(T)$ curves, due to the additional pinning introduced by the CD. Close to the defects ($\Theta = 28°$, shown with solid up triangles in the Fig. 14(b)) pinning is drastically increased.

In the virgin sample, curves at intermediate angles (e.g. $\Theta = 24.5°$, shown with solid up triangles in Fig. 14(a)) present a complicated structure. This characteristic structure extends to higher Θ as h_a decreases, occurring up to around 75° in the linear regime, as can be seen in the inset of Fig. 14(b). A similar behavior has been reported in recent works [67]. Generally, the sharp onset is related with a first order transition and the previous decrease in $\partial\chi'/\partial T$ is associated with a peak effect[68], although this last question is still open. Moreover, it has become clear by now that measurements in nonirradiated crystals at intermediate angles must be done taking into account the thermomagnetic history[67], so data at intermediate angles in Fig. 14(a) must be taken with caution. In any case, in the irradiated sample both the structure and memory effects disappear completely.

Data as those shown in Fig. 14 can be used to build up curves of $\chi' + 1$ as a function of Θ in both samples at fixed T. Figure 15 shows such curves at three different temperatures. Several features are apparent here. First, in the irradiated sample the original symmetry is broken ($\chi'(\Theta) \neq \chi'(-\Theta)$) by the presence of the tilted defects. This symmetry breaking occurs over a very large angular range; the symmetry is only recovered for $|\Theta| \geq \Theta_{sym} \sim 75°$, signaled with arrows in the figure. Second, in the asymmetric range $|\Theta| \leq \Theta_{sym}$ the screening of the ac field is, at any temperature, larger than the one corresponding to the virgin sample. Third, beyond $|\Theta_{sym}|$ the behavior of both samples is very similar.

The first obvious conclusion that arises from figure 15 is that pinning in the irradiated crystal is dominated by CD over most field orientations. It is apparent that the CD have a directional effect (*i.e.* they act as correlated pinning centers), as they modify the original symmetry. This is true even when $\mathbf{H_{dc}}$ is almost perpendicular to the tracks, between $-75°$ and $-60°$. Note also that, even in that angular region, the pinning due to the CD is much more efficient than that present in the non-irradiated sample, as indicated by the much

larger screening (smaller χ'). In the quadrant of positive Θ angles (the right side of the figures), where the track direction is included, the vortex pinning in the irradiated sample abruptly decreases around the Θ_{sym} angle, whereas in the left side, the screening falls down at $\Theta \sim -60^\circ$ and, not until 15° beyond this angle, at $\Theta \sim -\Theta_{sym}$, the behavior of the non-irradiated sample is recovered. In section III.E. we will show that the angle in which the screening falls down (for this case about -60°) is h_a dependent, and is a consequence of a change in the dynamical regime.

Figure 15 also shows that the response is not symmetric with respect to the defects direction. This fact can be easily explained since, as we argued in section II, the anisotropic character of the material and the presence of natural correlated defects (twin boundaries and *ab* planes) should have an important role in the structure of the vortices.

The main point to emphasize from these measurements is that the angular region in which the CD act as correlated pinning centers is very large. It can also be noticed that, in the range of temperature of Fig. 15, $\Theta_{sym} \sim 75^\circ$ is nearly constant. This behavior is not consistent with the existence of a trapping angle φ_T beyond which the correlated nature of the pinning should disappear, because at these high temperatures a such angle is expected to be very narrow and to decrease fast with T.

We now turn to the situation for field directions close to the *ab* planes ($|\Theta| > 75^\circ$). The very similar behavior of both samples in this angular region suggests that the main pinning source is the same. A related feature is that, in the non-irradiated sample, a qualitative change in the linear response is observed very near $\Theta \sim 75^\circ$ (inset of Fig. 14(a)). Beyond this angle, no structure is observed at any AC field. The above observations could be explained by assuming that Θ_{sym} indicates the angle beyond which, for both the irradiated and virgin samples, the *ab* planes become the prevailing pinning centers. However, due to the strong angular dependence of the AC response in the vicinity of the *ab* planes, it is clear that a similar study with a better resolution should be necessary to confirm the last conclusion.

It is useful at this point to compare and contrast these results with those obtained by DC magnetization, described in section II. A clear coincidence is that both sets of results show that correlated pinning dominates for all field orientations. The various angular regimes are related to different vortex structures arising from the combined effects of CD, twins and *ab* planes, not to crossovers to uncorrelated-pinning-dominated regimes. It is also true that, both near the Bose-glass transition and deep into the solid phase, over most field orientations vortices form staircases with segments pinned into the CD. The comparison of the Θ_{sym} obtained by both techniques is particularly interesting. The similarity of the values (see figs. 8, 9 and 15) strongly suggests that the underlying physics is similar. On the other hand, we should look carefully at the meaning of Θ_{sym} in each case. In the dc magnetization studies, our interpretation is that for $\Theta > \Theta_{sym}$ most of the kinks (which connect the vortex core segments pinned by the CD) are locked into the *ab* planes. This implies that intrinsic pinning must be important in that angular range. The ac data on Fig. 15 additionally suggest that at that high temperature intrinsic pinning may be *the dominant* pinning source in that range, as the ac response of the crystals with and without CD is the same. As this is not so clear at lower temperatures, more detailed studies of the interplay of CD and intrinsic pinning near Θ_{sym} as a function of temperature should be performed. Finally, it is worth to mention that, as expected, no evidence of lock-in phase or misalignment between $\mathbf{B}$ and $\mathbf{H_{dc}}$ is observed at the high temperatures of the ac studies.

Once the overall angular dependence of the ac response has been determined, we can

use the ac susceptibility measurements to explore in detail the various dynamic regimes that occur at a given field orientation as a function of T and H_{dc}, so a more microscopic information of the vortex-defects interactions can be obtained. Basically, this is achieved by changing the amplitude of the vortex oscillations, which are determined by the amplitude h_a. By performing these studies at a few selected orientations we can identify differences among the various angular regions, as will be shown in the next two subsections.

C. Dynamic regimes of vortices pinned by aligned columnar defects.

In this section we concentrate in the ac dynamic response when vortices are aligned to the columnar defects (*i.e.* $\varphi = 0$). By varying the amplitude and frequency of the ac field, we are able to cover a wide range of current densities. At the lowest amplitudes we observe the linear response with very low dissipation, characteristic of the oscillation of pinned vortices inside the tracks (Campbell regime)[6, 66], while at the high J limit a critical state develops. In between, a large non-linear transition regime is observed. We explore both the intra- and inter-valley dynamics in the same experiment, and we construct the dynamic phase diagram of the system in the T vs. h_a plane. We will present results for two irradiated samples. One of them is the sample A used in the previous section. The other one (sample C), was irradiated with 280 MeV Sb^{22+} at an angle of 15° from the c axis to a dose equivalent to $B_\phi \sim 3000$ Oe.

1. Linear response

A *linear regime* is characterized by a χ independent of h_a. By analyzing both components χ' and χ'' we are able to establish the nature of the regime. The linear ac susceptibility χ due to vortex motion in a superconductor is determined[48, 69, 70, 71] by the complex penetration depth $\lambda_{AC}(T, B, \omega) = \lambda_R + i\lambda_I$. The ratio $\varepsilon = \lambda_I/\lambda_R$, identifies several linear regimes. An ohmic response (*i.e.* a real resistivity) such as flux flow or thermally assisted flux flow (TAFF) corresponds to $\varepsilon = 1$. A *real* λ_{AC} ($\varepsilon = 0$) represents a non-dissipative response with $\chi'' = 0$, which is almost the case in the Campbell regime where *pinned* vortices perform *intra-valley* oscillations, although there is always some residual dissipation, thus $\varepsilon \ll 1$ but finite.

Our experimental situation is well approximated by a thin disk in a transverse ac magnetic field where, according to Brandt [48],

$$\chi' + 1 + i\chi'' = \sum_{n=1}^{N} c_n/(\Lambda_n + \varphi) \tag{8}$$

Here $\varphi = R\delta/2\pi\lambda_{AC}^2$, where R and δ are the disk radius and thickness respectively, c_n and Λ_n are tabulated real constants, and the sum arises from the discretization involved in the numerical procedure. Expression 8 allows us to calculate $\chi'(\lambda_R, \varepsilon)$ and $\chi''(\lambda_R, \varepsilon)$. We can numerically invert this function to compute $\lambda_R(T)$ and $\varepsilon(T)$ from our $\chi(T)$ data in the linear regime [72]. Figure 16 shows $\varepsilon(T)$ so obtained in sample A for $\mathbf{H_{dc} = 360}$ Oe parallel to the tracks. We observe that $\varepsilon(T)$ remains small and approximately constant, $\varepsilon \sim 0.1$,

for $T \leq 91.3K$. This behavior is characteristic of trapped vortices oscillating inside their pinning wells. At $T \sim 91.3$ K an abrupt depinning occurs, as indicated by the sudden increase in ε which in a narrow temperature range of ~ 0.2 K grows close to $\varepsilon = 1$ that corresponds to the ohmic (flux flow) regime.

It can be seen from Eq. (8) that, when $\varepsilon \ll 1$ (low dissipation limit), χ' is solely determined by the real part of the penetration depth, λ_R. On the other hand, $\lambda_R^2(T,B) = \lambda_L^2(T) + \lambda_C^2(T,B)$, where λ_L and λ_C are the London and Campbell penetration depths respectively[69, 70], being

$$\lambda_C^2(T,B) = \frac{B\Phi_0}{4\pi\alpha_L} \tag{9}$$

where α_L is the Labusch parameter that measures the restoring force of the pinning well.

Thus, measurements of $\chi(T)$ in the Campbell regime at various H_{dc} allows us to obtain $\lambda_C(T, B \sim H_{dc})$ and $\alpha_L(T, B \sim H_{dc})$. Figure 17 shows λ_R^2 vs. $H_{dc} \sim B$ at various temperatures in both samples. In sample C (figure 17(a)), $B_\phi \sim 360$ Oe without increasing the vortex density. It can be seen from figure 17(a) that, in sample C, $\lambda_C^2 \propto H_{dc} \approx B$, so Eq. (9) implies a field-independent α_L. This important result strongly suggests that vortices are individually pinned. The last interpretation is well supported by results in the sample A (figure 17(b)): at low dc fields λ_R^2 grows linearly with H_{dc}, but above $H_{dc} \sim 400$ Oe $\sim \frac{1}{2}B_\phi$ there is a faster increase of λ_R^2 with H_{dc}, indicating that α_L decreases with B. We interpret this feature as the crossover to a collective Campbell response. The values of α_L obtained in both samples are very similar, demonstrating that the field-independent α_L indeed characterize the elementary vortex- tracks interaction in a single vortex pinning regime.

We also detect a small dissipative component, frequency independent within our resolution, and which is likely to originate in thermally induced jumps between two metastable states of similar energy (two level systems) that characterizes a *glassy phase*[73]. We will not extend on this topic here, but refer to Ref. 72 for more details.

2. The onset of nonlinearity

As h_a increases, the response becomes nonlinear. In crystals with aligned CD the crossover from linear to nonlinear response is very smooth, so the exact boundary $h_a^l(T)$ between both regimes is difficult to determine and consequently we adopted an experimental criterion explained in ref. 32. This boundary signals the appearance of vortex oscillations that are large enough to break the linear approximation in the vortex motion equation. This may originate either from intra-valley motion (breakdown of the parabolic approximation for the pinning potential at large oscillation amplitudes[6, 66]) or from the increase of nonlinear flux creep (inter-valley jumps) as J grows[69]. In either case, the decrease of the pinning energy as T increases implies that h_a^l should decrease with T, as indeed observed.

As the amplitude of vortex oscillations in the linear limit is proportional [69] to the local current density J, which is spatially inhomogeneous, the breakdown of the harmonic oscillations occur at different h_a in different parts of the sample. For a disk in a transverse field, the current distribution in the linear regime can be numerically calculated starting from the experimental values of $\chi'(T)$ and following the procedure described by Brandt [48]. The method allows us to estimate the actual current density $J(T, \rho, h_a)$, where ρ is the distance from the center of the disk. Since J is larger at the disk border ($\rho = R$), nonlinearities first

occur there, when the local current density reaches the value $J^l(T) = J(T, R, h_a^l(T))$. Using our experimental estimate of the crossover field $h_a^l(T)$, we can calculate $J^l(T)$ as shown in the inset of Figure 16. As h_a keeps growing the boundary of the Campbell regime moves inward into the disk.

We can also estimate the transverse displacement of the vortices near the edge of the sample (those that perform the largest oscillations), $u(\rho \sim R)$. In the linear regime, u is related with J in the same position through the simple form $(1/c)\,\phi_0\,J(\rho) \approx \alpha_L u(\rho)$. The vortex displacement at the edge of the sample when linearity breaks down, r_l, will be

$$r_l = \frac{1}{c}\frac{\phi_0}{\alpha_L(T)} J^l(T) \tag{10}$$

The radius r_l measures the range where the pinning potential $\varepsilon_p(r)$ can be well approximated by a parabola. Using values for $J^l(T)$ and $\alpha_L(T)$ calculated from the experimental data, we obtain $r_l \approx 50$ Å in the sample A (irradiated with Au ions), and $r_l \approx 25$ Å in the sample B (irradiated with Sn ions). These values have a striking coincidence with the observed radius of columnar defects r_D in each case[28]. It is somehow surprising that even at these high temperatures where $\xi > r_D$, and so no drastic change in $\varepsilon_p(r)$ is expected[4] at $r = r_D$, the method still provide us information on the real size of the tracks.

3. The Critical state

At the highest amplitudes, vortices perform large excursions outside the pinning wells and inter-valley motion will dominate over most of the sample. Above a lower boundary $h_a^c(T)$ the response is well described by a Bean critical state [45]. The large intermediate region $h_a^l(T) < h_a < h_a^c(T)$ corresponds to a crossover regime where both the intra-valley and inter-valley vortex motion contribute significantly to the ac response.

To define the lower boundary $h_a^c(T)$ of the critical state regime, we have developed an experimental method based in the analysis of the $\chi'(T, h_a)$ data[32]. We will not explain the method in detail here but only point out its basic concepts. The Bean Model assumes that there is an uniform persistent density current in any region of the sample where inter-valley vortex motion occurs. Due to flux creep effects, that current density J_ω is smaller than J_c and depends on the frequency of the measurement. This determines a frequency dependent Bean length

$$\Lambda_c(T, h_a) = \frac{c}{4\pi}\frac{h_a}{J_\omega(T)} \tag{11}$$

The screening component χ' is only a function of Λ_c divided by some characteristic sample dimension. The dependence of χ' on this dimensionless variable is shape-dependent and in general difficult to calculate. The key idea of the method is to identify data (at fixed frequency) at different T and h_a that combine to produce the same Λ_c according to Eq. (11). The consistency of the resulting function $\Lambda_c(h_a)$ is checked at each temperature. A critical state is established if, at constant T and ω, Λ_c turns out to be proportional to h_a.

Figure 18(a) shows the result of such analysis at several temperatures in sample A. In all cases we observe that $\Lambda_c \propto h_a$ at high amplitudes, thus proving the existence of a Bean regime. At low amplitudes there is a systematic deviation from a straight line and Λ_c becomes larger than expected in the Bean regime, indicating the absence of a fully developed

critical state. The field $h_a^c(T)$ that marks the onset of the Bean regime, is shown by arrows in Figure 18(a). Note that in the critical state regime $d\Lambda_c/dh_a \propto 1/J_\omega(T)$, thus the variation of the slope of Λ_c vs. h_a with T (which appears as a vertical shift in the log-log plot of Figure 18(a)) allows us to determine the *temperature dependence* of $J_\omega(T)$.

The great advantage of the above procedure is that it allows us to test the existence of a Bean regime, to determine its limits in the $h_a - T$ plane and to obtain the temperature dependence of $J(T)$ *regardless of the sample geometry*. The function $\chi'(\Lambda_c)$ is unique to each sample, although, as expected, we found[32] that the general shape is similar for different YBCO crystals with similar aspect ratio.

To estimate the absolute values of J we need to estimate the absolute values of Λ_c, and to that end we must rely on some geometrical modeling. We use the result[47] for a thin disk in a transverse field, $\chi' = 0.5$ when $\Lambda_c/\delta = 0.75$. In the right axis of Figure 18(a) we indicate the actual values of Λ_c obtained in adopting such criterion. The corresponding values of the persistent current density (identified as $J_{90kHz}(T)$ to emphasize that it is frequency dependent) are shown in Figure 16. The numerical estimates of $\Lambda_c(T)$ and $J(T)$ may be affected by a systematic error because our sample is not a disk, but the difference will be an overall factor of the order of unity and is irrelevant within the context of our analysis.

Inspection of Figure 16 shows that the persistent current vanishes very close to the temperature where the Campbell regime disappears and ε in the linear limit starts to grow. The coincidence of both facts identify the *Bose glass* transition temperature T_{BG}. In the inset of figure 16, we can see that the temperature dependence of the persistent current density J_{90kHz} in the critical state closely follows that of $J^l(T)$, the limiting current of the linear regime. This observation implies that the linearity of the intra-valley oscillations in the Campbell regime is lost when the current density at the sample perimeter reaches a significant fraction ($\sim 20\%$) of the current density that flows in the critical state.

As mentioned above, the dynamics in this limit is strongly affected by flux creep, thus the persistent current density J is much smaller than the critical current density J_c . Measurements at different frequencies allow us to determine the temperature and current density dependence of the activation energy, $U(J,T)$ in a wide range of J. We have devised[32] a procedure to extract this information from the frequency dependence of the $\chi(T)$ curves in the critical state. Figure 18(b) shows the main result from this study. There is a characteristic glassy behavior $U(J) = J^{-\alpha}$ (see section I.C.). At large current densities $U \propto J^{-1.5}$, the exponent progressively decreasing at low J. A dynamic exponent $\alpha = 1.5$ is typical of collective creep of vortex bundles[4, 74]. Blatter *et al.* [4] predict this dependence in the regime of large bundles, *i.e.*, for transverse bundle dimension larger than λ_L. (The decrease of α at low J could indicate a crossover to a charge density wave (CDW)-type creep regime). We also observe a very strong T dependence[32], consistent with creep of vortex bundles at high temperature.

4. Dynamic diagram

From the above analysis, it is possible to build up a diagram in the (h_a, T) plane to identify the various dynamic regimes and analyze the crossovers among them. Figure 19 shows a such diagram, for the sample A at $H_{dc} = 360$ Oe parallel to the CD, and $f = 90$ kHz. The response for $T \leq 91.2$ K is characteristic of pinned vortices in a glassy phase. Below the crossover field $h_a^l(T)$, we observe a regime of pinned vortices performing intra-valley oscillations inside their pinning sites. The ac susceptibility is well characterized by a

Campbell penetration depth and a small dissipative component. Above a second line $h_a^c(T)$ (and again for $T \leq 91.2$ K), a Bean critical state forms. The persistent current density flowing in this regime is determined by thermally activated processes that involve inter-valley collective jumps of vortex bundles. In between these two extreme regimes there is an intermediate nonlinear region that occupies a large portion of the (h_a, T) plane, as $h_a^l(T)$ and $h_a^c(T)$ differ by more than one order of magnitude as seen in the Figure.

Within the temperature range $T \sim 91.2 - 91.3$ K both the Campbell and Bean critical regimes disappear. This is indicative of a sudden depinning of vortices at a Bose-glass transition that occurs in the range 91.2 K $\leq T_{BG} \leq$ 91.3 K. Above 91.3 K, the behavior is indicative of a vortex liquid. A linear response is observed for $h_a \leq 25$ mOe, but the dissipation grows rapidly approaching an ohmic response ($\varepsilon = 1$) at $T \sim 91.5$ K (see Figure 16). However, at high h_a we still observe a nonlinear response, *i.e.*, we cannot access experimentally the unpinned (ohmic) liquid region. This is probably because at our low H_{dc} the unpinned liquid regime only occurs in a very narrow temperature range below T_c.

Let's now analyze the glassy phase of the dynamic diagram in terms of existing models for vortex motion. According to the simplest scenario[69], the crossover between Campbell and Bean critical regimes should occur at a field $h_a^*(T)$ where the range of field penetration in the later (which is proportional to h_a) becomes larger than the range of field penetration in the former (which is independent of h_a). For a longitudinal geometry (e.g., a slab or cylinder in a parallel field) this leads to the simple crossover condition $\Lambda_c(h_a, T) \sim \lambda_R(T)$ but, in our case, a meaningful comparison should involve the actual field penetration ranges rather than the penetration depths. The practical criterion that we have adopted is to consider that the range of field penetration in the linear and critical regimes is the same when $\chi' = -1/2$ in each case. This crossover should occur when $\left(\sqrt{(2R/\delta)}/3\right)\Lambda_c(T) \sim \lambda_R(T)$, *i.e.*, according to Eq. (11), when

$$\lambda_R(T) \sim \frac{c}{4\pi}\left[\frac{1}{3}\sqrt{\frac{2R}{\delta}}\right]\frac{h_a^*(T)}{J(T)} \tag{12}$$

We can use Eq. (12) to estimate the crossover field $h_a^*(T)$ from $\lambda_R(T)$ and $J(T)$. We emphasize that $\lambda_R(T)$ and $J(T)$ are obtained in totally independent ways; the former from the linear regime data (section III.C.1) and the latter from the high h_a data using the geometrical procedure described in section III.C.3. The result is shown in Figure 19: the theoretical expectation for the crossover field $h_a^*(T)$ coincides very well with the line $h_a^c(T)$ that indicates the formation of a Bean critical state. This good agreement supports the validity of the basic concept, *the critical state develops when the Bean penetration range becomes longer than the Campbell penetration range.*

We now discuss the origin and nature of the large intermediate regime. The observation of a nonlinear response at current densities well below J_{90KHz}, the current density flowing in the Bean critical state, indicates that these nonlinearities are associated with intra-valley oscillations. This can be understood by considering the shape of the pinning potential, that at these high temperatures is rather shallow. For the present crystal we found in section III.C.2 that nonlinearities develop when the amplitude of the oscillations at the sample border reaches a value $u(\rho = R) = r_l \sim 50$ Å. We associate r_l with the range where the pinning potential $\varepsilon_p(r)$ can be well approximated by a parabola, which is smaller than the total pinning range. This picture explains the smooth nature of the crossover from linear to nonlinear response at $h_a^l(T)$.

As was discussed in section I.C., in the temperature and field range of our ac measurements we are deep into the collective pinning regime. This is in agreement with the conclusion of section III.C.3. However, the linear response in the Campbell regime is well described by a field independent Labusch parameter characteristic of single vortex pinning (section III.C.1). This apparent contradiction is easily resolved when the size of the vortex displacements involved in each case are taken into account. The linear response corresponds to oscillations that are uniform along the field direction, whose amplitude $\left(\leq 50\mathring{A}\right)$ is much smaller than the vortex lattice parameter $a \sim 2100$ Å. In this range of displacements the energy variation sensed by a vortex due to the elastic interaction with the neighbor vortices is negligible as compared to the variation of the pinning energy, and thus the response is solely determined by the interaction of a single vortex with the tracks. We note, however, that the transverse localization length is much longer than the defect separation, thus each vortex is collectively pinned by many defects. The amplitude of the oscillations refers to the vortex center of mass, and the effective pinning potential arises from the contribution of more than one track. In the critical state regime at high amplitudes, on the other hand, the inter-valley vortex excitations involve transverse displacements of the order of the defect separation or larger, and consequently the vortex-vortex interactions play a fundamental role in the response.

D. Dynamic regimes in tilted vortices.

In this section we use the methods described above for aligned CD, to complete the study of the angular dependence presented in section III.B with a detailed analysis of the AC dynamic regimes at various orientations of $\mathbf{H_{dc}}$. We will use the same irradiated crystal (sample A, $\Theta_D = 30°$). The angles selected are representative of the various angular regions: $\mathbf{H_{dc}}$ forming an angle very small relative to defects ($\Theta \sim 34°$, $\varphi \sim 4°$), $\mathbf{H_{dc}}$ along the symmetric direction of tracks relative to the c axis ($\Theta \sim -30°$, $\varphi \sim -60°$), and $\mathbf{H_{dc}}$ in the angular region where the screening fall down ($\Theta \sim -70°$, $\varphi \sim 80°$). For comparison, we also include the response with aligned vortices ($\Theta \sim 30°$, $\varphi \sim 0°$) and the analogue response of the virgin crystal (sample B) for $\Theta \sim 30°$. In all cases, the response at very low AC fields is linear, and it becomes non-linear above a threshold AC field $h_a^l(\Theta, T)$. In the following subsection we compare the results obtained in the linear regime for each one of the chosen angles, and later we analyze the non-linear response.

1. Linear regime

We have used the procedure explained in section III.C.1 to obtain the linear real penetration depth and the Labusch constant in the linear regime. To analyze the B dependence of α_L, we performed measurements for several values of DC fields along the chosen directions in the linear regime, and we calculated the corresponding $\lambda_R^2(\chi')$. We have observed qualitative differences in the behavior in the various angular ranges.

In figure 20 various curves of $\lambda_R^2(B)$ for the chosen values of Θ are compared at $T = 90.5$ K. We can see that the qualitative $\lambda_R^2(B)$ behavior observed when $\mathbf{B}$ is aligned with the tracks still holds if the field is tilted by a few degrees ($\Theta = 34°$), but it changes notably for larger tilts, and it is also very different in the non-irradiated sample. In the last two

cases, no linear dependence in λ_R^2 vs. B at low fields is observed, indicating that a Labusch constant independent of field does not exist. It can be seen that the Campbell penetration length λ_C is much shorter when $\mathbf{H_{dc}} \parallel$ CD than for angles far away (4 or 5 times) and than for the non-irradiated sample (10 times). For fields higher than $B_\phi/2$, the ratio between the Campbell lengths in different orientations decreases.

Furthermore, we observe that the response at $\Theta = -30°$ in the irradiated sample is different to the one observed at $\Theta = 30°$ in all the range of measured fields; this means that up to $H_{dc} \approx 2B_\phi$ the presence of defects is still important. A noteworthy result is that, for low DC fields, the responses at $-70°$ and $-30°$ are very similar. For $\Theta = -30°$ near $H_{dc} = B_\phi/2$, the curve starts to increase more swiftly, and both responses can be clearly distinguished. This fact indicates that even at an angle $\varphi \sim -60°$ from the tracks direction, the occupation of defects play an important role.

The above experimental results can be qualitatively understood as follows. In section III.B. we concluded that vortices are partially accommodated in the defects for all the chosen angles. The restitutive constant α_L is higher in the vortex segments that are accommodated in the columnar defects. For this reason, while the Campbell regime remains individual, the average Labusch constant will increase with the length of pinned segments, *i.e.* when the angle φ (relative to defects) decreases. For large φ the situation is more complex: the fraction pinned by the tracks is very small (it can be seen that α_L for the non-irradiated sample at 30° is just half the value observed at $-30°$ in the irradiated sample). Moreover, the pinning force for small displacements is comparable to that induced by neighbor vortices and α_L is no longer independent of B.

2. Nonlinear response

Measurements in all the available range of h_a have been performed. The first notable observation is that, in the non linear regime, the angular dependence of the AC response is much more pronounced than in the linear regime. For large angles relative to the CD, as soon as the linear behavior is lost the $\chi(T)$ curves get wider in temperature and the dissipation peaks notably increase. These facts are resumed in figure 21, where the non linear behavior at different angles and their comparison with the non-irradiated sample are shown. In figure 21(a), various $\chi'(h_a)$ curves at the same temperature (90.5 K) for different angles are plotted, while in figure 21(b) all the curves included have the same λ_R (and therefore they were obtained at different temperatures).

It can be observed that the AC field h_a^l at which loss of linearity occurs is lower when the pinning due to the CD is less efficient: in the non-irradiated sample (solid down triangles in the figures), h_a^l is almost one order of magnitude lower than in the case of the irradiated sample with field aligned to defects (open squares in the figures). When $\mathbf{H_{dc}} \parallel$ CD, departure from linearity is smooth, while for large φ angles (solid circles and open up triangles in the figures) the departure from linearity is much more abrupt.

The dependence of χ on h_a for the highest h_a is also very different. Whereas in the case of aligned columnar defects this function can be explained in the framework of a critical state model, for large φ angles this dependence decreases tending to a new linear regime. This behavior is still more notable in the non-irradiated sample. Consistently with the last observation the maximum of $\chi''(T)$ approaches the expected values[48] for the ohmic regime ($\chi''_{\max} \sim 0.44$ for a disk in transversal geometry). The last remark is displayed in figure

22. There we compare experimental points of χ'' vs. $\chi' + 1$ obtained at different angles at $h_a \sim 6.4$ Oe, with those calculated for a disk both in the Bean critical state (continuous line in the figure) and in the ohmic regime (dashed line). While in the irradiated sample the response at $\Theta = 30°$ is similar to the expectation for a critical state, for angles far away from the defects it tends to the ohmic behavior. Notice that, as well as $\chi''_{\max}$ increases, $\chi'(\chi''_{\max})$ also tends to the expected value in a linear ohmic regime.

As another test to close this picture, we tried to check whether a critical state regime is established or not, applying the procedure presented in section III.C.3 to data obtained at $\Theta = -70°$. A satisfactory solution was not attained, proving that those data are not consistent with the critical state model.

A possible explanation for this behavior is the following: When φ is large, the effective critical current density J_ω is much lower than in the case in which $\mathbf{H_{dc}}$ is aligned with the tracks. In fact, it is so much reduced that a critical state cannot be established: as soon as the linearity is lost, and the vortex displacements become mainly determined by creep mechanisms across the pinning centers, the AC field penetration length increases very much, and becomes comparable to the flux flow skin depth. In this condition, a nonlinear regime in which pinning forces, activated mechanisms and viscous losses contribute significantly to the vortex motion is established.

Finally, another interesting consideration arises from figure 21, as it allows us to re-analyze the angular dependence of $\chi(\Theta)$ previously shown in section III.B, figure 15. The angle beyond which there is an abrupt increase in the AC field penetration in the left side of figure 15 ($\Theta \approx -60°$), corresponds to the angle for which, at the particular AC field value $h_a = 0.2$ Oe, the system changes from a nearly linear regime to a non linear one. This fact can be easily verified crossing the curves $\chi'(h_a)$ at $h_a = 200$ mOe in figure 22(a). By performing the same procedure at lower h_a we can observe that, if angular measurements were made at lower AC fields, a smooth angular dependence would extend to orientations closer to the *ab* planes. On the other hand, if we perform the procedure for $h_a = 400$ mOe, the abrupt increase of AC field penetration will appear before $\Theta = -30°$. For even higher values of h_a, the region drastically affected by the CD will only involve the peak close to the defects, as it has been reported previously [44]. From all this considerations, we point out that the apparent angular region notably affected by the CD is h_a dependent. Thus, results of angular measurements performed using only using AC amplitude, without characterizing the dynamic regimes involved, should be interpreted with caution.

IV. CONCLUSION

High temperature superconductors with correlated disorder provide a fascinating framework for the exploration of novel ideas on vortex physics. In addition, our understanding of this topic will be essential for the optimization of YBCO superconducting wires for technological applications, as vortex motion in those materials is also dominated by correlated pinning, arising in that case from fabrication-dependent microstructures.

We have explored in detail the angular dependent vortex dynamics in type II superconductors with aligned columnar defects introduced by irradiation with very energetic heavy-ions. We have used dc magnetization measurements deep in the vortex solid phase, and ac susceptibility near the solid-liquid transition. We have shown that aligned columnar defects are an excellent tool to test models for vortex dynamics, particularly if they are tilted with respect to the crystallographic axes, so their effects can be easily distinguished from those

arising from mass anisotropy, sample geometry, twin boundaries and intrinsic pinning. This allows us, for instance, to use the uniaxial pinning of the columnar defects as a probe to determine the orientation of the vortices inside a bulk material, which in general is different from the orientation of the applied fields.

In some aspects we have found an excellent agreement with the theoretical expectations of the Bose-glass model. The field dependence of the lock-in angle follows remarkably well the $1/H$ prediction over the whole temperature range of our measurements. In turn, the temperature dependence of the lock-in angle gives strong support to the concept of an effective pinning energy dominated by the entropic smearing effect. On the other hand, both our ac and dc results show that columnar defects produce effective pinning over a wide angular range, and that correlated pinning dominates the scenario for all field orientations. One consequence of this is the existence of a rich variety of vortex staircases, with segments locked into different correlated structures.

The complexity of the picture is even larger when the high temperature dynamics is taken into account. When the magnetic field is aligned with the tracks the ac susceptibility at low ac excitations exhibits a linear response arising from vortices oscillating inside the tracks, which is characterized by a Labusch parameter independent of the dc field. This indicates that the response is dominated by the individual vortex-track interaction, even though the critical current in the same temperature and field range is determined by collective pinning mechanisms. The solution of this paradox is related to the fact that the characteristic size of the vortex displacements in each case is very different. Finally, the ac response at different angles indicates that the characteristics of the dynamic regimes and their extension in the temperature vs ac field plane are strongly dependent on the orientation of the vortices with respect to both the columnar defects and the crystalline structure.

V. ACKNOWLEDGEMENTS

We are pleased to thank the Atomic Energy Commission of Argentina, where all the measurements presented in this review have been performed. We also want to thank the CONICET of Argentina for financial support. The experimental results described in this review were obtained in collaboration with H. Lanza, G. Nieva, P. Levy, M. Avila, D. Niebieskikwiat, S. Candia and D. Casa. We acknowledge many valuable discussions with V. Bekeris, G. Blatter, F. de la Cruz, D. Lopez, J. Guimpel, A. Herbsommer, L. Krusin-Elbaum, J.R. Thompson, and S. Valenzuela.

---

[1] L. Civale, A. D. Marwick, T. K. Worthington, M. A. Kirk, J. R. Thompson, L. Krusin-Elbaum, Y. Sun, J. R. Clem, F. Holtzberg, Phys. Rev. Lett. **67**, 648 (1991).

[2] M. Konczykowski, F. Rullier-Albenke, E. R. Yacoby, A. Shaulov, Y. Yeshurum, and P. Lejay, Phys. Rev. B **44**, 7167 (1991).

[3] D. R. Nelson and V. M. Vinokur, Phys. Rev. Lett. **68**, 2398 (1992); Phys. Rev. B **48**, 13060 (1993).

[4] G. Blatter, M. V. Feigel'man, V. B. Geshkenbein, A. I. Larkin and V. M. Vinokur, Rev. Mod. Phys. **66**, 1125 (1994).

[5] See, e.g., L. Civale, Supercond. Sci. Technol. **10**, A11-A28 (1997); L. Civale, in *Processing and Properties of High-Temperature Superconductors*, ed. Sungho Jin (World Scientific Publishing Co.) Vol. **1** (1993), and references therein.
[6] See, e.g., A. M. Campbell and J. E. Evetts, Adv. Phys. **21**, 199 (1972).
[7] I. V. Grigorieva, L. A. Gurevich, and L. Y. Vinninkov, Physica C **195**, 327 (1992).
[8] W. K. Kwok *et al.*, Phys. Rev. Lett. **64**, 966 (1990); S. Fleshler *et al.*, Phys. Rev. B **47**, 14448 (1993).
[9] Y. H. Li, A. A. Menovsky, and J. M. Franse, Phys. Rev. B **48**, 6612 (1993).
[10] M. Oussena, P. A. J. de Groot, S. J. Porter, R. Gagnon and L. Taillefer, Phys. Rev. Lett. **76**, 2559 (1996).
[11] A. A. Zhukov, G. K. Perkins, J. V. Thomas, A. D. Caplin, H. Küpfer, and T. Wolf, Phys. Rev. B **56**, 3481 (1997).
[12] M. Tachiki and S. Takahashi, Solid State Commun **70**, 291 (1989).
[13] W. K. Kwok, U. Welp, V. M. Vinokur, S. Fleshler, J. Downey, and G. W. Crabtree, Phys. Rev. Lett. **67**, 390 (1991); W. K. Kwok, J. Fendrich, U. Welp, S. Fleshler, J. Downey, and G. W. Crabtree, Phys. Rev. Lett. **72**, 1088 (1994).
[14] J. Mannhart, D. Anselmetti, J. G. Bednorz, A. Catana, Ch. Gerber, K. A. Muller, and D. G. Schlomm, Z. Phys. B: Condens. Matter **86**, 177 (1992).
[15] B. Dam, J. M. Huijbregtse, F. C. Klaassen, R. C. F. van der Geest, G. Doornhos, J. H. Rector, A. M. Testa, S. Freisem, J. C. Martinez, B Staube-Pumpin, and R. Griessen, Nature (London) **399**, 439 (1990); J. M. Huijbregtse, B. Dam, R. C. F. van der Geest, F. C. Klaassen, R. Elberse, J. H. Rector, and R. Griessen, Phys. Rev. B **62**, 1338 (2000) and references therein.
[16] B. Maiorov and E. Osquiguil, Phys. Rev. B **64**, 052511 (2001).
[17] G. Kreiselmeyer, M. Müller, M. Kraus, B. Holzapfel, S. Bouffard, and G Saemann-Ischenko, Physica C **235-240**, 3055 (1994).
[18] L. Krusin-Elbaum, A. D. Marwick, R. Wheeler, C. Feild, V. M. Vinokur, G. K. Leaf, and M. Palumbo, Phys. Rev. Lett. **76**, 2563 (1996).
[19] R. L. Fleischer, H. R. Hart, K. W. Lay, and F. E. Luborsky, Phys. Rev. B **40**, 2163 (1989).
[20] L. Krusin-Elbaum, J. R. Thompson, R. Wheeler, A. D. Marwick, C. Li, S. Patel, D. T. Shaw, P. Lisowski, and J. Ullman, Appl. Phys. Lett. **64**, 3331 (1994); H. Safar, J. H. Cho, S. Fleshler, M. P. Maley, J. O. Willis, J. Y. Coulter, J. Ullman, G. N. Riley, M. W. Rupich, J. R. Thompson and L. Krusin-Elbaum, Appl. Phys. Lett. **67**, 130 (1995).
[21] F. de la Cruz, D. Lopez and G. Nieva, Philos. Mag. B **70**, 773 (1994).
[22] C. A. Bolle, F. de la Cruz, P. L. Gammel, J. V. Wasczak, and D. J. Bishop, Phys. Rev. Lett. **71**, 4039 (1993).
[23] G. P. Summers, E. A. Burke, D. B. Chrisey, M. Nastasi, and J. R. Tesmer, Appl. Phys. Lett. **55**, 1469 (1989).
[24] B. Hensel, B. Roas, S. Henke, R. Hopfengärtner, M. Lippert, J. P. Ströbel, M. Vildic, and G. Saemann-Ischenko, Phys. Rev. B **42**, 4135 (1990).
[25] M. A. Kirk and H. W. Weber, in *Studies of High-Temperature Superconductors*, ed A. V. Narlikar (Nova Science Publishers Inc., New York), Vol. **10** (1992), and references therein.
[26] G. Fuchs, F. Studer, E. Balanzat, D. Groult, M. Toulemonde, and J. C. Jousset, Europhys. Lett. **3**, 321 (1987).
[27] F. Studer and M. Toulemonde, Nucl. Instr. Meth. B **65**, 560 (1992).
[28] A. D. Marwick, L. Civale, L. Krusin-Elbaun, R. Wheeler, J. R. Thompson, T. K. Worthington, M. A. Kirk, Y. R. Sun, H. R. Kerchner and F. Holtzberg, *Proceeding of the 8th International*

Conference of Ion Bean Modification of Material, Haildelberg, Germany (1992).
[29] L. Civale, L. Krusin-Elbaum, J. R. Thompson, R. Wheeler, A. D. Marwick, M. A. Kirk, Y. R. Sun, F. Holtzberg, and C. Feild, Phys. Rev. B **50**, 4102 (1994).
[30] L. Krusin-Elbaum, L. Civale, J. R. Thompson and C. Feild, Phys. Rev. B **53**, 11744 (1996).
[31] L. Civale, G. Pasquini, P. Levy, G. Nieva, D. Casa and H. Lanza, Physica C **263**, 389 (1996).
[32] G. Pasquini, L. Civale, H. Lanza and G. Nieva, Phys. Rev. B **59**, 9627 (1999).
[33] D. Niebieskikwiat, L. Civale, C.A. Balseiro and G. Nieva, Phys. Rev. B **61**, 7135 (2000).
[34] T. Hwa, P. LeDoussal, D. R. Nelson, and V. M. Vinokur, Phys. Rev. Lett. **71**, 3545 (1993).
[35] D. Niebieskikwiat, A. Silhanek, L. Civale and G. Nieva, Phys. Rev. B **63**, 144504 (2001).
[36] A. Mazilu, H. Safar, M. P. Maley, J. Y. Coulter, L. N. Bulaevskii, and S. Foltyn, Phys. Rev. B **58**, 8909 (1998).
[37] Z. Yao, S. Yoon, H. Dai, S. Fan, and C. M. Lieber, Nature **371**, 777 (1994).
[38] K. Harada, T. Matsuda, J. Bonevich, M. Igarashi, S. Kondo, G. Pozzi, U. Kawabe, and A. Tonomura, Nature **360**, 51 (1992).
[39] A. Tonomura, H. Kasai, O. Kamimura, T. Matsuda, K. Harada, Y. Nakayama, J. Shimoyama, K. Kishio, T. Hanaguri, K. Kitazawa, M. Sasase, and S. Okayasu, Nature **412**, 620 (2001).
[40] W. K. Kwok, S. Fleshler, U. Welp, V. M. Vinokur, J. Downey, G. W. Crabtree and M. M. Miller, Phys. Rev. Lett. **69**, 3370 (1992).
[41] L. Klein, E. R. Yacoby, Y. Wolfus, Y. Yeshurun, L. Burlachov, B. Ya Shapiro, M. Konczykowski and F. Holtzberg, Phys. Rev. B **47**, 12349 (1993); L. Klein, E. R. Yacoby, Y. Wolfus, Y. Yeshurun, L. Burlachov, B. Ya Shapiro, M. Konczykowski and F. Holtzberg, Phys. Rev. B **48**, 3523 (1993).
[42] B. Holzapfel *et al.*, Phys. Rev. B **48**, 600 (1993).
[43] V. Hardy, A. Wahl, S. Hébert, A. Ruyter, J. Provost, D. Groult and Ch. Simon, Phys. Rev. B **54**, 656 (1996).
[44] A. Herbsommer, J. Luzuriaga, L. Civale, G. Pasquini and G. Nieva, Physica C **304**, 112 (1998).
[45] C. P. Bean, Phys. Rev. Lett. **8**, 250 (1962).
[46] J. M. Däumling and D. C. Larbalestier, Phys. Rev. B **40**, 9350 (1989).
[47] J. R. Clem and A. Sanchez, Phys. Rev. B **50**, 9355 (1994).
[48] E. H. Brandt, Phys. Rev. B **49**, 9024 (1994); *ibid.*, **50**, 4034 (1994); *ibid.*, **52**, 15442 (1995); *ibid.*, **50**, 13833 (1994).
[49] L. W. Conner and A. P. Malozemoff, Phys. Rev. B **43**, 402 (1991).
[50] E. M. Gyorgy, R. B. van Dover, K. A. Jackson, L. F. Schneemeyer and J. V. Waszczak, Appl. Phys. Lett. **55**, 283 (1989).
[51] F. Hellman, E. M. Gyorgy and R. C. Dynes, Phys. Rev. Lett. **68**, 867 (1992).
[52] A. A. Zhukov, G. K. Perkins, Yu. V. Bugoslavsky and A. D. Caplin, Phys. Rev. B **56**, 2809 (1997).
[53] T. Schuster, H. Khun, M. R. Koblischa, H. Theuss, H. Kronmüller, M. Leghissa, M. Kraus and G. Saemann-Ischenko, Phys. Rev. B **47**, 373 (1993); T. Schuster et al. Physica C **203**, 203 (1992); T. Schuster et al. Phys. Rev. B **52**, 10375 (1995).
[54] T. Tamegai, L. Krusin-Elbaum, P. Santhanam, M. J. Brady, C. Feild and F. Holtzberg, Phys. Rev. B **45**, 2589 (1992).
[55] D. V. Shantsev, Y. M. Galperin, and T. H. Johansen, Phys. Rev. B **61**, 9699 (2000).
[56] A. V. Silhanek, L. Civale, S. Candia, G. Nieva and G. Pasquini, Phys. Rev. B, **59**, 13620 (1999).

[57] A.V. Silhanek, D. Niebieskikwiat, L. Civale, M. Avila, O. Billoni and D. Casa, Phys. Rev. B **60**, 13189 (1999).
[58] M. A. Avila, L. Civale, A. V. Silhanek, R. A. Ribeiro. O. F. de Lima and H. Lanza. Phys. Rev. B **64**, 144502 (2001).
[59] R. Prozorov, A. Poddar, E. Sheriff, A. Shaulov, and Y. Yeshurun, Physica C **264**, 27 (1996).
[60] D. H. Kim, C. W. Lee, T. W. Lee, H. R. Lim, and I. S. Kim, Phys. Rev. B **64**, 184518 (2001).
[61] G. Blatter, V. B. Geshkenbein and A. I. Larkin, Phys. Rev. Lett. **68**, 875 (1992).
[62] A.V. Silhanek and L. Civale. Physica C, Vol. 341-348(1-4) pp.1227-1228 (2000).
[63] E. H. J. Morré, Ph.D. thesis, Instituto Balseiro (1997); E. H. J. Morré *et al.*, Phys. Lett. A **233**, 130 (1997).
[64] A.V. Silhanek, L. Civale, and M.A. Avila Phys. Rev. B **65**, 174525 (2002).
[65] P. de Trey, Suso Gygax, and J.-P. Jan, Journal of Low Temperature Physics **11**, 421 (1973).
[66] A. M. Campbell, J. Phys. C **4**, 3186 (1971).
[67] S. O. Valenzuela and V. Bekeris, Phys. Rev. Lett. **84**, 4200 (2000).
[68] W. De Sorvo, Rev. Mod. Phys. **36**, 90 (1964); W. K. Kwok, J. A. Fendrich, C. J. van der Beek and G. W. Crabtree, Phys. Rev. Lett. **73**, 2614 (1994).
[69] C. J. van der Beek, V. B. Geshkenbein and V. M. Vinokur, Phys. Rev. B **48**, 3393 (1993).
[70] M. W. Coffey and J. R. Clem, Phys. Rev. B **45**, 9872 (1992).
[71] E. H. Brandt, Physica C **195**, 1 (1992).
[72] G. Pasquini, P. Levy, L. Civale, G. Nieva, and H. Lanza, Physica C **274**, 165 (1997).
[73] A. E. Koshelev and V. M. Vinokur, Physica C **173**, 465 (1991).
[74] M. Konczykowski, V. M. Vinokur, F. Rullier-Albenque, Y. Yeshurun and F. Holtzberg, Phys. Rev. B **47**, 5531 (1993); M. Konczykowski, Physica C **209**, 247 (1993).

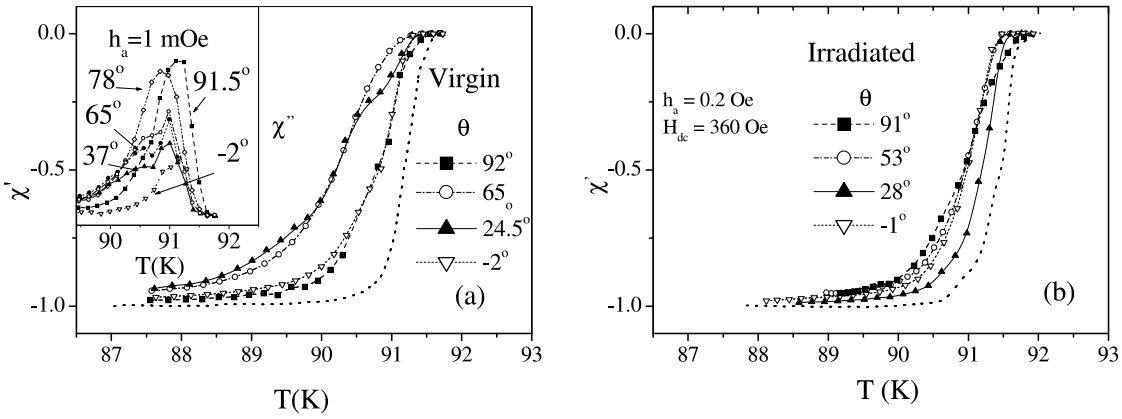

FIG. 14: a) Temperature dependence of the out-of-phase component χ' of the ac susceptibility with $\mathbf{H_{dc}}$ oriented at various angles Θ relative to the c axis in a nonirradiated sample. Inset: curves of χ'' as a function of T in the linear regime; a structure is present at intermediate angles. b) Same in a sample irradiated with a matching field $B_\phi = 700$ Oe at $\Theta = 30°$.

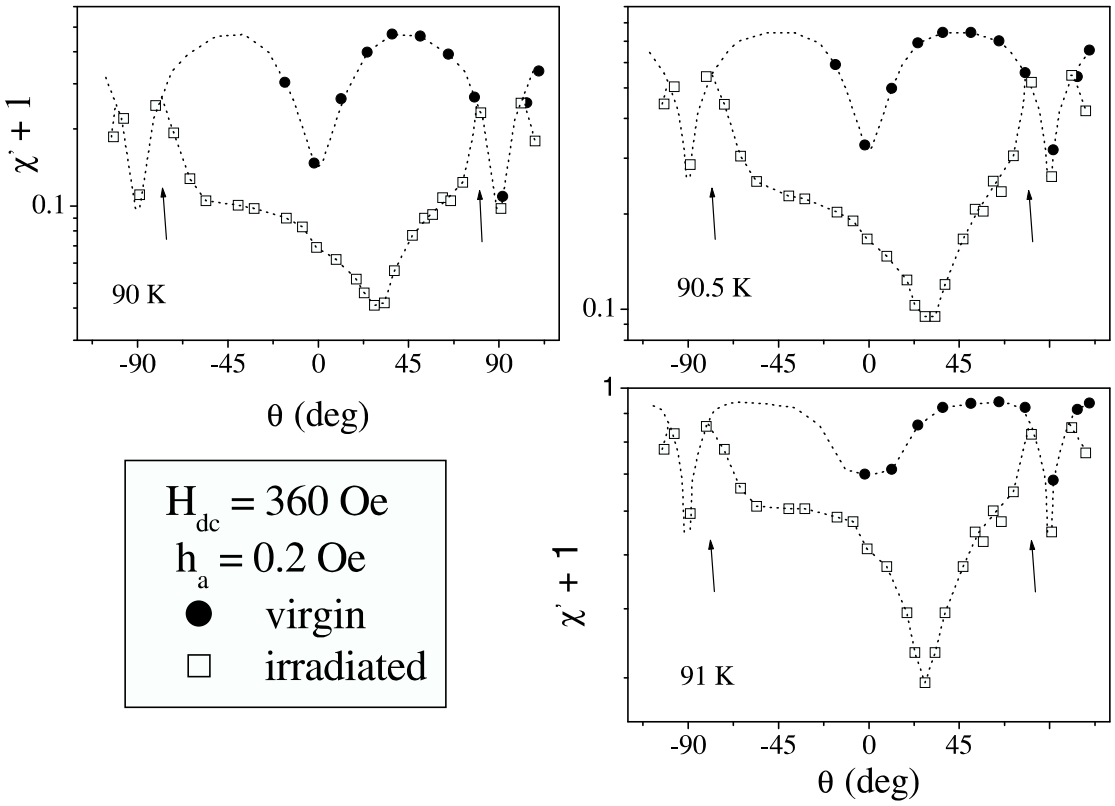

FIG. 15: Angular dependence of $\chi' + 1$ in an irradiated (open squares) and virgin sample (circles) at different temperatures. The dotted lines are guide to the eye (in the virgin sample it has been

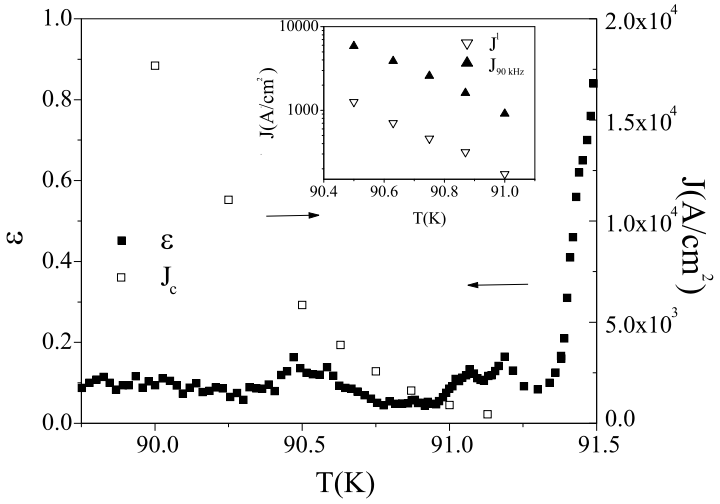

FIG. 16: Temperature dependence of ε=λ_I/λ_R, where λ_{ac}=iλ_I+λ_R is the penetration depth in the linear regime, and J_{90kHz} is the frequency dependent current density in the Bean regime for f=90 kHz. At T=91.3 K there is a sudden increase in ε towards the ohmic regime and J_{90kHz} vanishes. The inset shows in semi logarithmic scale the temperature dependence of J_{90kHz} and J^l, the limiting current of the linear regime.

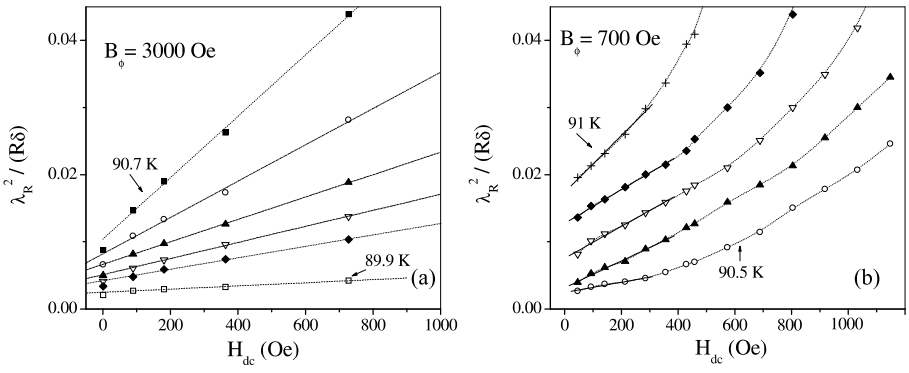

FIG. 17: Field dependence of the square of the dimensionless linear real penetration depth at various temperatures in two irradiated samples with different doses. If $B \lesssim B_\phi/2$, a linear dependence holds.

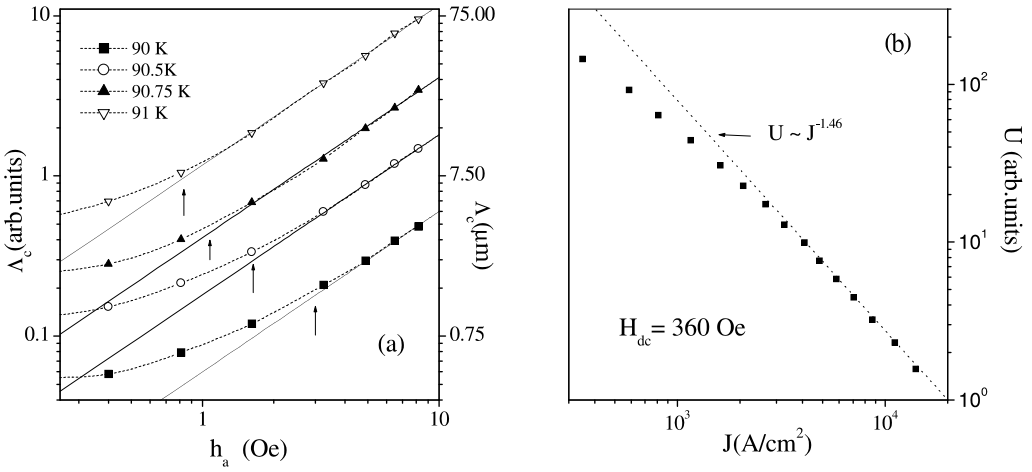

FIG. 18: (a) Test that proves the existence of a critical regime. The Bean length Λ_c is proportional to h_a above $h_a^c(T)$ signaled by the arrows. (b) Current density dependence of the activation energy. The U values came from the frequency dependence of χ' in the critical state.

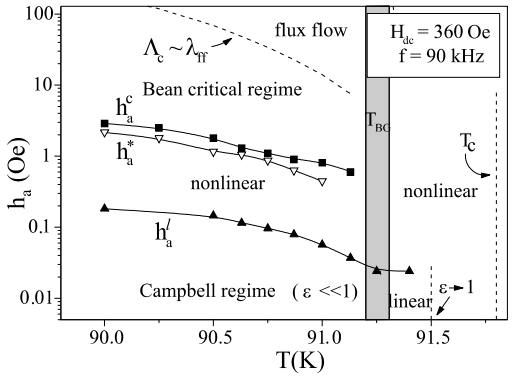

FIG. 19: Dynamic diagram in the (h_a, T) plane for an irradiated sample with $B_\phi = 700$ Oe.

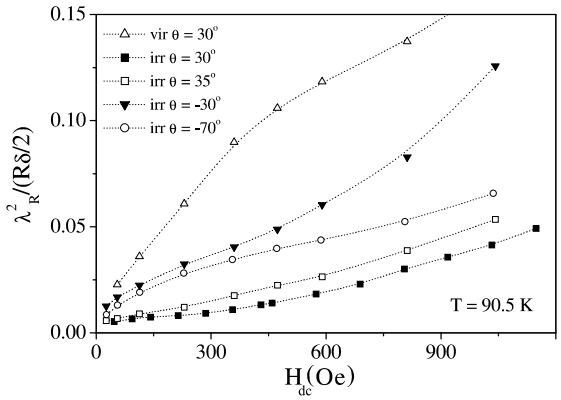

FIG. 20: Field dependence of the square of the dimensionless linear real penetration depth in an irradiated sample at a fixed temperature for different angles Θ. A curve of a virgin sample is also shown.

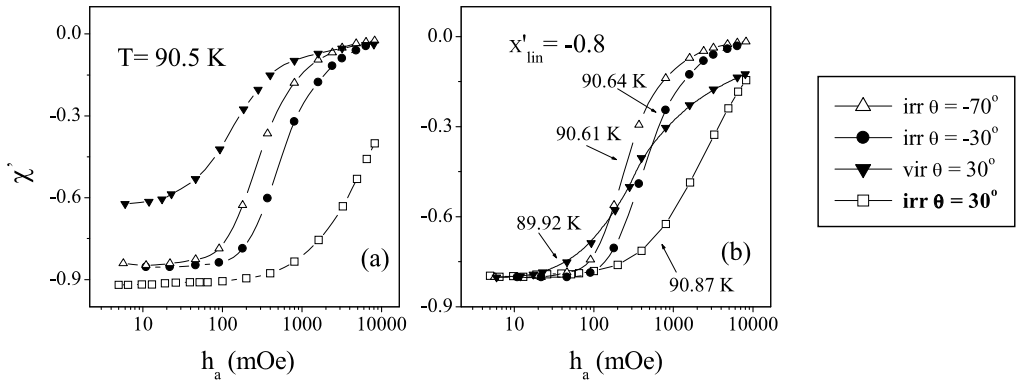

FIG. 21: Linear and nonlinear behavior at different angles Θ as a function of the ac field. (a) Comparison of $\chi'(h_a)$ curves at the same temperature. (b) Comparison at the same linear real penetration depth. Symbols correspond to both panels.

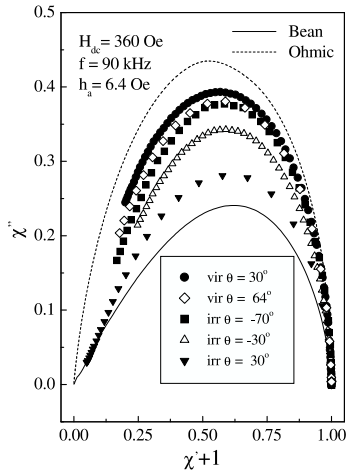

FIG. 22: Experimental curves $\chi''(\chi')$ at a large $h_a = 6.4$ Oe in the irradiated an virgin sample for various angles. Lines are the theoretical calculation for a disk in an Ohmic regime (dashed line) and in a Bean critical state (solid line).

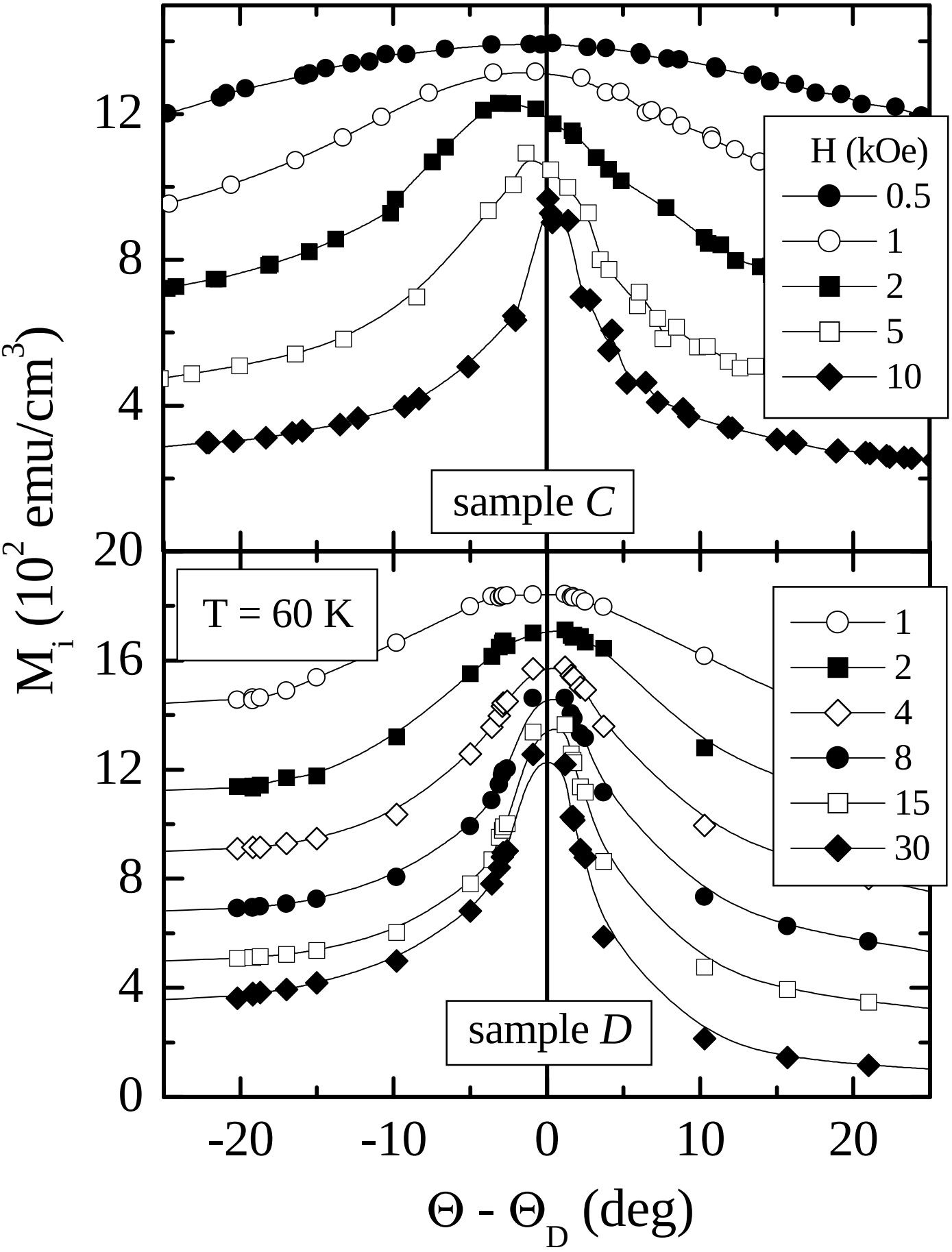
H (kOe)
0.5
1
2
5
10
sample C
T = 60 K
1
2
4
8
15
30
sample D
M_i (10^2 emu/cm^3)
Θ - Θ_D (deg)
0
4
8
12
16
20
-20
-10
0
10
20